SANDIA REPORT

SAND2004-1415
Unlimited Release
Printed April, 2004

Autonomous Microexplosives Subsurface Tracing System Final Report

N.R. Warpinski, B.P. Engler, J.E. Uhl, M.C. Grubelich, S.H. Kravitz, J. Nogan, R.R.Rivas,P.W. Cooper, G.R. Dulleck, B.V. Ingram, and B.M. Melof

Prepared by
Sandia National Laboratories
Albuquerque, New Mexico 87185 and Livermore, California 94550

Sandia is a multiprogram laboratory operated by Sandia Corporation,
a Lockheed Martin Company, for the United States Department of Energy's
National Nuclear Security Administration under Contract DE-AC04-94AL85000.

Issued by Sandia National Laboratories, operated for the United States Department of Energy by Sandia Corporation.

Available to DOE and DOE contractors from
U.S. Department of Energy
Office of Scientific and Technical Information
P.O. Box 62
Oak Ridge, TN 37831

Telephone: (865)576-8401
Facsimile: (865)576-5728
E-Mail: reports@adonis.osti.gov
Online ordering: http://www.doe.gov/bridge

Available to the public from
U.S. Department of Commerce
National Technical Information Service
5285 Port Royal Rd
Springfield, VA 22161

Telephone: (800)553-6847
Facsimile: (703)605-6900
E-Mail: orders@ntis.fedworld.gov
Online order: http://www.ntis.gov/help/ordermethods.asp?loc=7-4-0#online

SAND2004-1415
Unlimited Release
April 2004

Autonomous Microexplosives Subsurface Tracing System Final Report

Norman R. Warpinski, Bruce P. Engler and James E. Uhl
Geophysical Technology Department

Mark C. Grubelich
Advanced Concepts Group

Stanley H. Kravitz, John Nogan
Microdevice Technologies Department

Raul R. Rivas and Paul W. Cooper
Explosive Applications Department

George R. Dulleck
Integrated Microsystems Department

Brian V. Ingram and Brian M. Melof
Explosive Technologies Group

Sandia National Laboratories
P.O. Box 5800
Albuquerque, NM 87185-0750

Abstract

The objective of the autonomous micro-explosive subsurface tracing system is to image the location and geometry of hydraulically induced fractures in subsurface petroleum reservoirs. This system is based on the insertion of a swarm of autonomous micro-explosive packages during the fracturing process, with subsequent triggering of the energetic material to create an array of micro-seismic sources that can be detected and analyzed using existing seismic receiver arrays and analysis software. The project included investigations of energetic mixtures, triggering systems, package size and shape, and seismic output. Given the current absence of any technology capable of such high resolution mapping of subsurface structures, this technology has the potential for major impact on petroleum industry, which spends approximately $1 billion dollar per year on hydraulic fracturing operations in the United States alone.

Contents

Figures

Tables

This page intentionally left blank.

Introduction

The ability to actively image natural and man-made structures beneath the surface of the earth is limited by current technology requiring that energy sources and/or sensors be located either at the land surface or within boreholes penetrating the subsurface. Sandia is currently exploring the development of autonomous micro-explosive tracers that can be injected into subsurface fractures and through their subsequent explosive energy release provide the acoustic information necessary to map the exact geometry of the fracture system. The ability to perform such high resolution imaging is unprecedented and has the potential for major impacts in fossil energy, as well as a variety of other subsurface structure-characterization challenges such as subsurface waste injection, nuclear waste repository fast-transport-pathway identification, and hardened and deeply buried target location. The nearest term, highest impact arena for application of this technology is high resolution mapping of hydraulic fractures in the petroleum industry.[1-3]

Hydraulic fracturing is a critical hydrocarbon-extraction technology whereby long, penetrating fractures are created in gas and oil reservoirs by the injection of high-pressure, viscous fluids, supplemented by propping agents such as sand to keep the fractures open once pumping ceases. These fractures provide conduits for hydrocarbons to migrate faster and easier towards the wellbore for production and utilization. Out of the 20,000 to 30,000 wells drilled annually in the US, about 80% of them are hydraulically fractured, resulting in an over $1 billion industry that is absolutely essential to the continued economic vitality of the petroleum industry. Improvements in this technology could result in 10-20% cost savings in the fracturing operations and, more importantly, it could increase producible reserves by much larger factors and improve economics (thus spurring more drilling) by increasing the rate of return on the capital investment (by increasing initial production rates).

While the petroleum industry has a well-developed capability to create hydraulic fractures (e.g., pumps, tanks, blenders, fluids, propping agents, additives, etc.), the technology is far from optimized because of an inability to see, measure, or image the results of the created fracture. Important parameters such as length, height, azimuth, asymmetry, dip, width, distribution of propping agent, and other factors are unknown at the end of the “treatment”. The effectiveness of the treatment is usually deduced from the production of the resource from the well. Minimal diagnostic capabilities are currently available, generally limited to analyses of the injection pressure and some geophysical logs that provide information on fracture height at the wellbore. Sandia and others are working on two advanced concepts using micro-earthquake (or microseismic) monitoring and downhole tiltmeter monitoring, but these two technologies have limitations on what they can resolve and where they can be applied. In both cases, arrays of instruments are situated in nearby wells to respectively monitor the seismic and mechanical responses of the rock to the fracturing operation.[4]

The application of micro-explosive tracer technology to hydraulic fracture imaging builds on the microseismic monitoring technology by using the same seismic instrumentation and processing technology, but extends its applicability to all fracturing conditions by emplacing micro-explosive tracers that create small seismic sources distributed throughout the fracture. Locating the embedded explosive seismic sources will produce much higher spatial resolution, is not dependent on reservoir conditions (analyzable micro-earthquakes are not generated in some reservoirs), and marks the fracture directly. In addition, this system would allow the monitoring arrays to be used in the same well that is fractured; this single-well implementation is not currently possible and it severely restricts the use of monitoring technology.

As this technology develops and the micro-explosives are further enhanced and miniaturized, the application could be extended into any of the other injection operations performed by the petroleum

industry, such as waterflooding, drill-cuttings injection, gas-storage reservoir development, and FracPack completions (short, wide fractures in unconsolidated sandstones). Such a concept could be useful for any application where these tracers can be injected into fractures, fissures, pipes, or other openings and their final subsurface locations detected via a seismic array. Facilities such as mines, repositories, and structures could be characterized or detected in this manner.

This report details effort to develop an autonomous micro-explosive for use in hydraulic fracturing. It begins with an investigation of energetic materials that are likely to be suitable for this application, with particular emphasis on finding an energetic material that would react with water at a sufficiently rapid rate to produce a fast pressure pulse that would be imparted on the side walls of a hydraulic fracture. While a reaction between the energetic material and the water in the fracture (after dissolving or breaking a seal) is the simplest concept, a parallel study was also started to look at triggering devices. Such a trigger would use a semiconductor bridge (SCB) with some power source and timer or other sensor to fire the device at the appropriate time. Elements of package shape and flow through the fracture were also considered, as was the amount of energy that would be coupled into the rock (through simulations). Laboratory tests of the energetic materials were carried out to assess rise time and a concrete block test was designed to examine the pulse shape in the rock.

System Concept

The basic concept of the micro-explosive subsurface tracer is to use existing fracturing technology to (1) insert autonomous micro-explosive packages throughout the created hydraulic fracture, (2) have those packages function [i.e. trigger and explode] under appropriate conditions, (3) detect the induced seismic energy with available seismic receiver arrays, and (4) use conventional processing techniques to determine the source location, thereby marking the fracture. Thus, the new micro-explosive technology can be quickly integrated with available technology infrastructure. As shown in Figure 1, the pumps, wellbore and created fracture are part of the existing hydraulic-fracture process and the only new operation would be injection of micro-explosive packages into the flow stream. Once downhole, the packages would be carried along with proping agent by the viscous fluids used in routine fracturing operations and dispersed throughout the fracture.

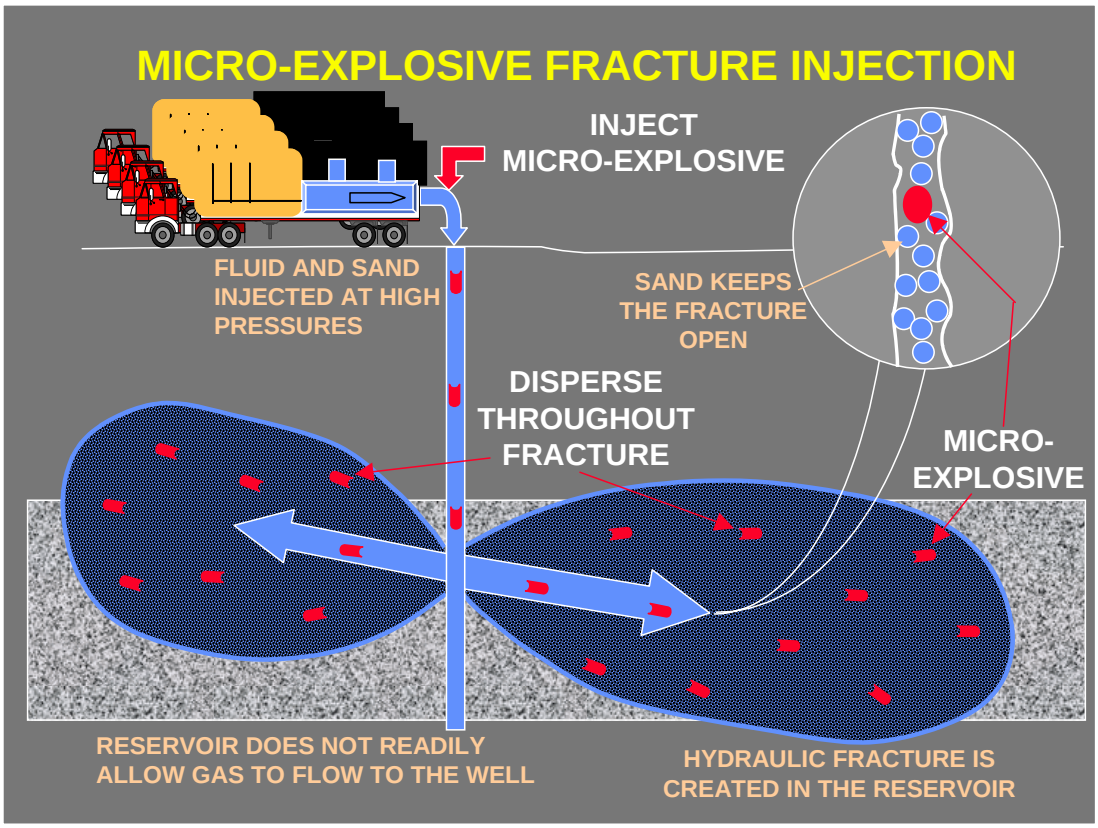

Figure 1. Micro-explosive tracer injection into fracture system

The packages would be designed and built so that they function at appropriate times or under appropriate environmental conditions (e.g., timer, pressure switch, reaction with fluid) and have sufficient energy and rise time to produce detectable seismic waves. Important considerations are the type of energetic material, the triggering mechanism, and the packaging needed to survive in the harsh environment (high pressure, somewhat elevated temperature, highly abrasive, aqueous conditions). To fit in the fracture, the micro-explosive packages would need to be quite small, but they could have a shaped design with a small cross-sectional area, as the non-Newtonian fracturing fluids generally have sufficient elasticity (relative to the inertial forces) to turn elongated particles into the flow stream.

Once emplaced, the micro-explosive packages would need sufficient delay so that they function under optimum conditions. If seismic receivers are in an offset well, an optimum time would be an hour or two after the fracture when the noise generated by the fracturing and the moving fluids had decayed and the explosive event would be most easily detected. For seismic receivers run in the "treatment" well, the optimum time would be several hours to as much as a day, the time necessary to clean up the well and run the receiver array downhole.

The seismic receiver array would consist of a multi-level array of tri-axial accelerometers spaced correctly to span the interval that was fractured.[4] These instruments would be run continuously for several hours to detect the ensemble of micro-explosive events. Available automatic processing would find the events and triangulate on the source locations, minimizing the work needed to process the results. The final output would be a 3D image or 2D plan-view and side-view images of the fracture length, height, azimuth and other geometric features. The monitoring system is shown schematically in Figure 2.

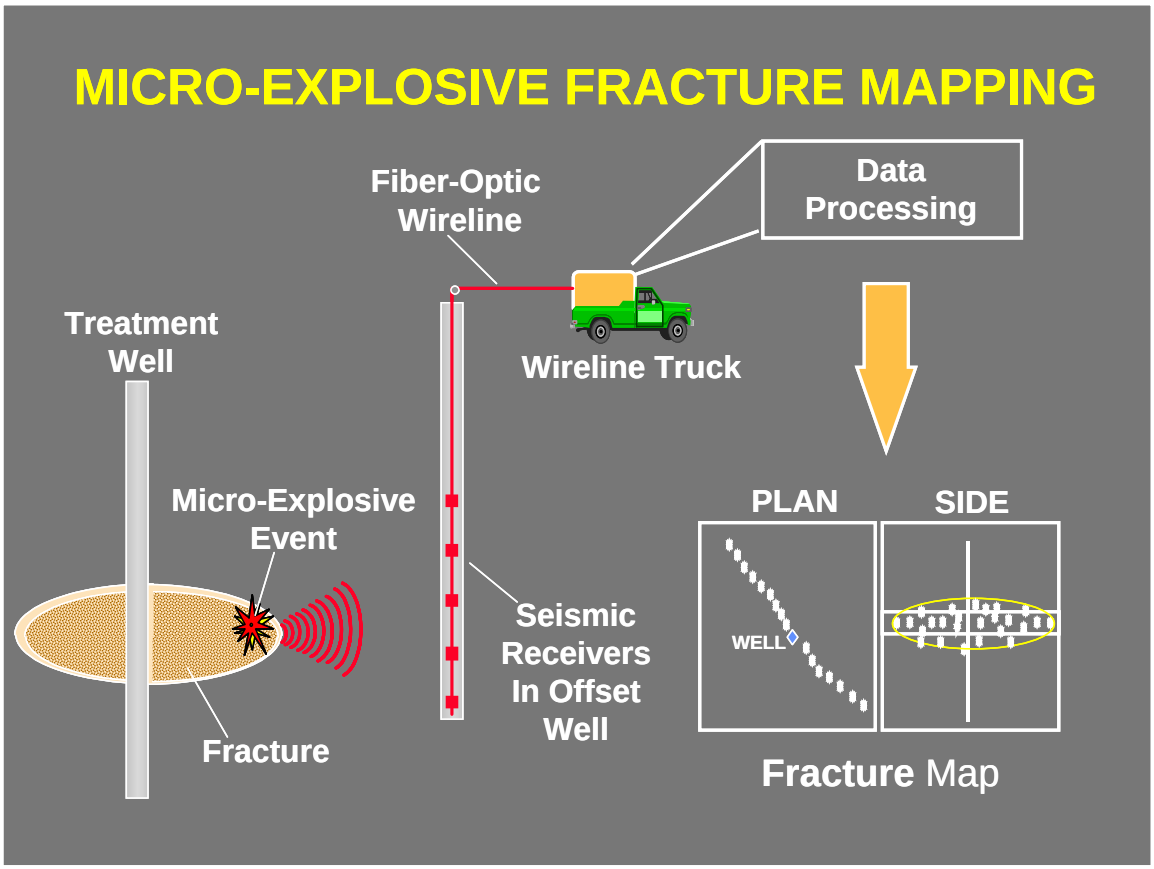

Figure 2. Micro-explosive fracture mapping

Theoretical calculations and experimental data from borehole-based explosives indicate that sufficient energetic material can be encapsulated in a small enough volume to be injected into a fracture and detected at a reasonable sensing distance.

In order to realize the micro-explosive tracer technology, the following key research questions must be addressed:

- *How small a seismic signal can be detected and analyzed?* Is the explosive energy from a micro-explosive package, coupled with the rock and energy transmission, sufficient to produce an interpretable signal?

- *Can the energetic material be appropriately "functioned"?* Can the explosive packages be triggered at appropriate times and under appropriate conditions, and will it generate an energy release that produces the right shape of seismic source within fracture/rock materials?

- *Can the packages be made small enough?* Can sufficient volume of energetic material and a reliable trigger mechanism be stuffed into a package that is small enough to inject during the hydraulic fracturing process?

Triggering Mechanisms and Energetic Materials

Preliminary analyses have identified three combinations of triggering mechanism and energetic materials. Development and testing of these alternatives is a primary research objective.

The first alternative is reaction of the package with the down-hole environment to directly initiate the energetic event. Primary elements in the hydraulic fracture environment are: pressure, temperature, and water. Water with a high chloride content will attack and dissolve a corrosion rupture disk. When this disk ruptures, water will rapidly enter the package, which will contain a small pellet of alkali metal. Being highly reactive, the alkali metal will spontaneously oxidize and produce hydrogen gas. This reaction will result in a mild explosion.

The second alternative is an electrically activated ignition of either a pyrotechnic or a primary energetic material. The pyrotechnic material of choice is THKP [titanium subhydride potassium perchlorate]. The primary energetic material of choice is CP [2-(5-Cyanotetrazolato) pentaamminecobalt (III) perchlorate]. The electrical activation would be accomplished using a miniature semiconductor bridge [SCB]. This Sandia invention is far superior to a hot wire ignition source because it uses much less energy.

A miniature SCB can be custom designed and fabricated at the bottom of a small cavity in a silicon device. This cavity will be loaded with either pyrotechnic or primary energetic material. When as little as 30 micro joules of energy is imposed on the SCB, a gas plasma is created that initiates the energetic reaction. The small amount of energy used for ignition is easily available from miniature battery technology. If necessary, a small capacitor could be integrated into this system. Triggering of this system can be accomplished by using a timer, sensing high pressure and/or elevated temperature, or by closing a switch after a rupture disk allows water to enter as in the first alternative.

The third alternative is a combination of the triggering mechanism from the first alternative and the energetic material from the second. A rupture disk could be used to allow water to initiate a combustion reaction between two chemicals [such as metallic magnesium and silver nitrate] producing a strong exothermic reaction. The heat from this reaction can be used to initiate an explosion in a primary or pyrotechnic material.

Tracer Package Design and Emplacement in Hydraulic Fracture Environments

The size of the package is limited to a fraction of the fracture width (1-30 mm), but it must contain a resistant exterior coating, the necessary volume of explosive material, and any additional circuitry, batteries, capacitors, corrosion disks, etc. needed for timing and triggering. Corrosion disk design and hermetic sealing need special investigation to provide assurance that a rugged, but inexpensive package will be attainable. To maximize the amount of explosive and allow for the triggering mechanism, tracer packages would likely be given an appropriate elongated shape. While such a shaped package would normally turn crosswise and bridge in the flow of a Newtonian fluid through a fracture, the non-Newtonian nature of typical fracturing fluids will generally align the long side of the packages with the flow stream, allowing them to flow through the fractures. Proper design will require evaluation of the package shapes versus fluid properties and determination of which combinations of elasticity number (ratio of elastic-to-viscous forces) and shape characteristics are applicable. For fracturing operations with Newtonian fluids (about 30% of all fractures), spherical particles would need to be designed. For some operations in poorly consolidated sands (FracPacks[5]), larger spherical particles would also be appropriate as the fracture widths are quite large in these treatments.

Energetic Material Evaluation

Most of the project effort has been devoted to finding an energetic material that will act as a primer mix to initiate a detonation. Such a material would ideally have a burn rate that is optimized for generating seismic energy in the desired frequency range for maximum detectability using accelerometer sensors in down-hole receiver arrays. As a part of determining material characteristics, a test chamber was constructed for evaluating burn characteristics and a Henkin test apparatus was built to evaluate material behavior.

Test Chamber

In order to test the various concepts of microexplosive functioning in a confined environment, an apparatus was constructed in which to test material response. This apparatus is essentially a test chamber that is built to withstand the high pressure and dynamic loading of an explosive event, albeit a relatively small one. The test chamber was built to hold an autonomous microexplosive package, control the functioning of that package, and record the output of the subsequent event. The chamber is 10 inches inside diameter and 10 inches long, built of stainless steel with a design pressure rating of 5,000 psi and is shown in Figure 3. The end plates of the chamber are 2-inch-thick stainless steel attached with eight bolts, as shown in Figure 4. The top end plate has a plunger unit and a pellet section attached to it that allows for the safe insertion of micro-explosive pellets. This piece is shown in Figure 5. The plunger unit is shown in more detail in Figure 6 and the pellet section is shown in Figure 7.

The chamber can be used in many modes, but the first mode to be considered is that of reactive substances. The test chamber is built with an attached isolation disk (in the pellet section) that holds the reactive material between burst plugs. A compressed-air-driven ram (the plunger unit) pushes the material into the test chamber, allowing it to react with the resident fluid. To record the output of the package, pressure sensors are attached to the apparatus to record the subsequent waveform and rise time. The compressed-air ram is controlled remotely, as well as a drain valve to bleed pressure after the test.

Figure 3. Test section of chamber

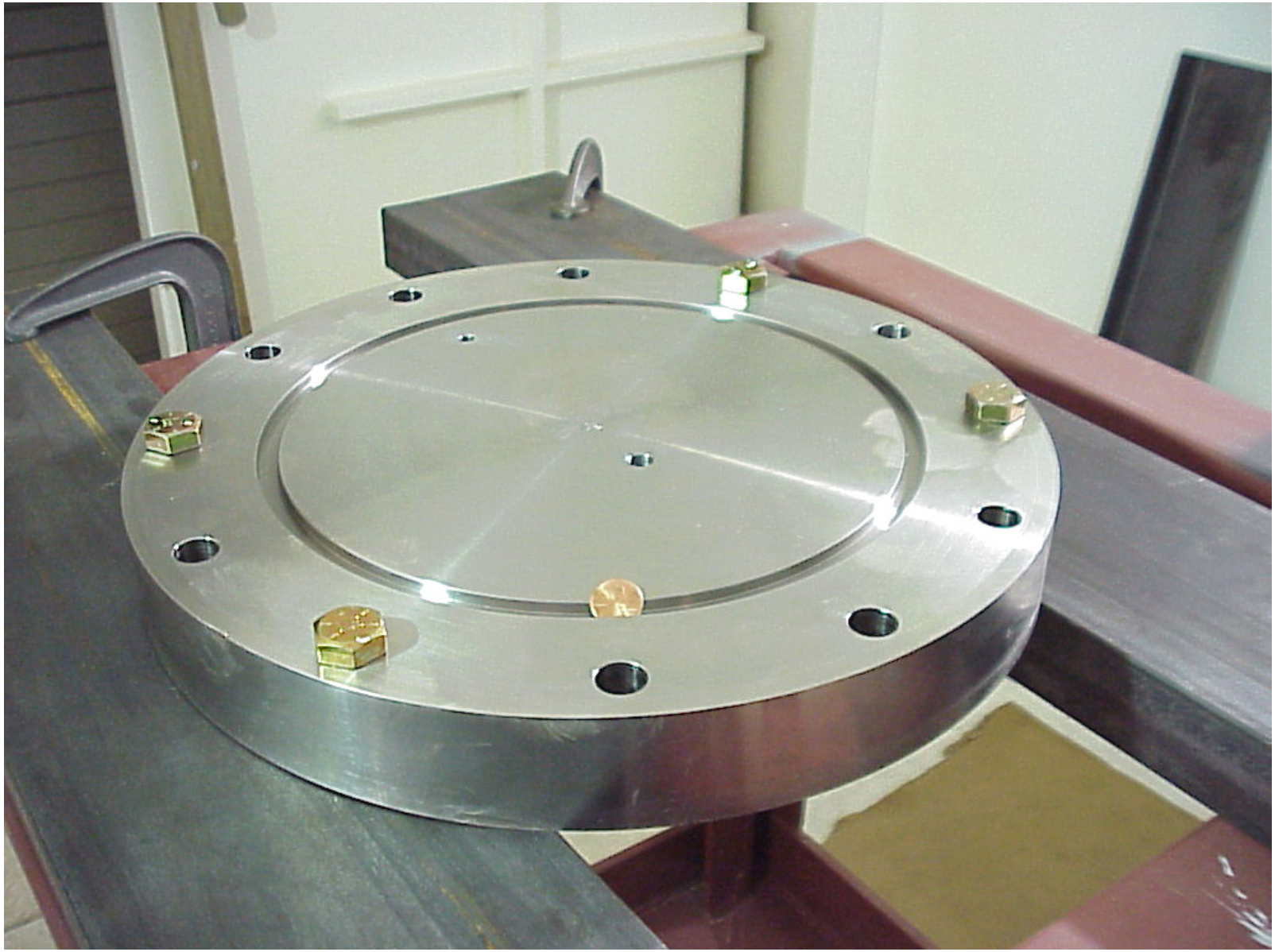

Figure 4. Bottom plate of chamber

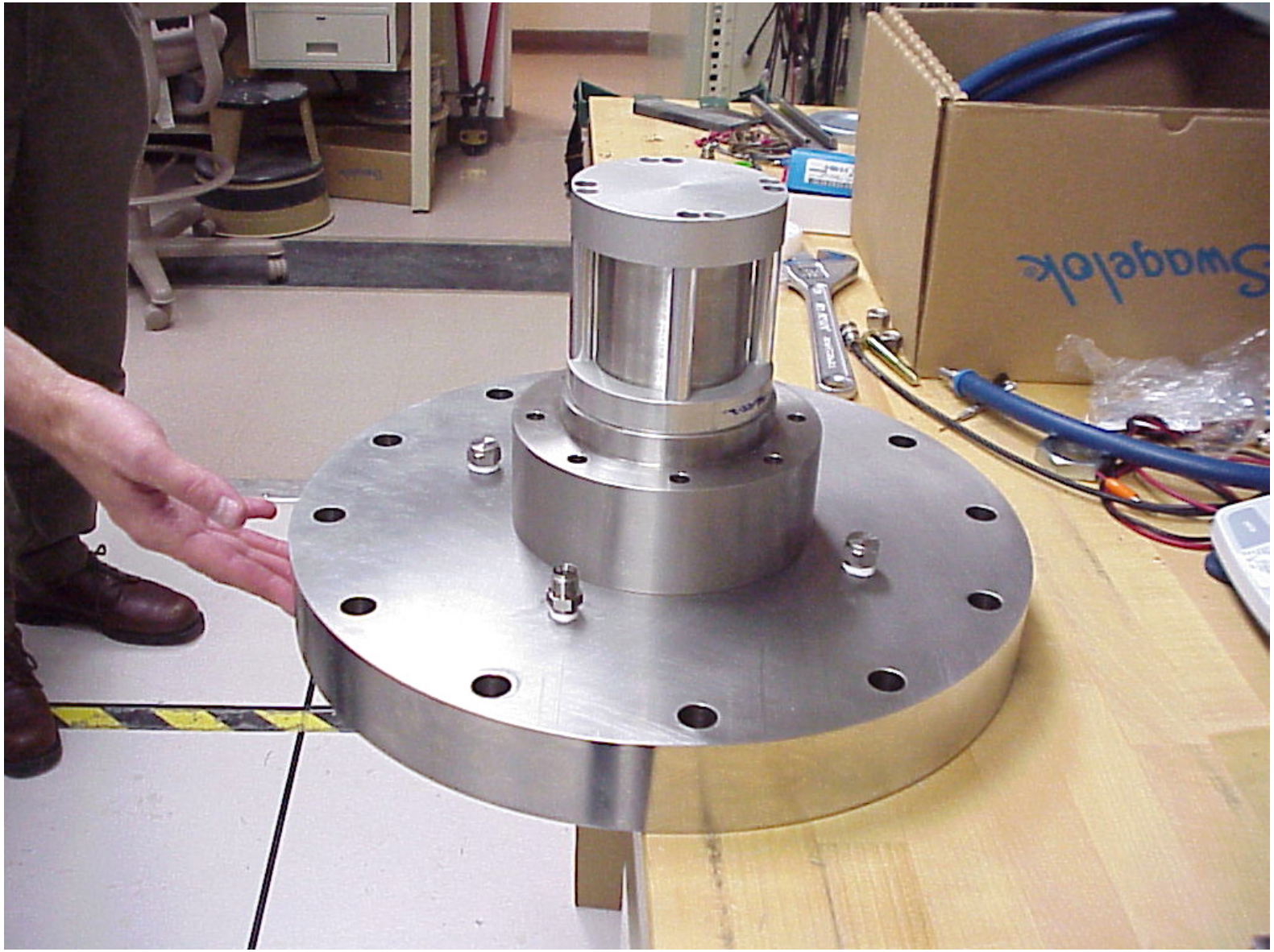

Figure 5. Top end plate of chamber

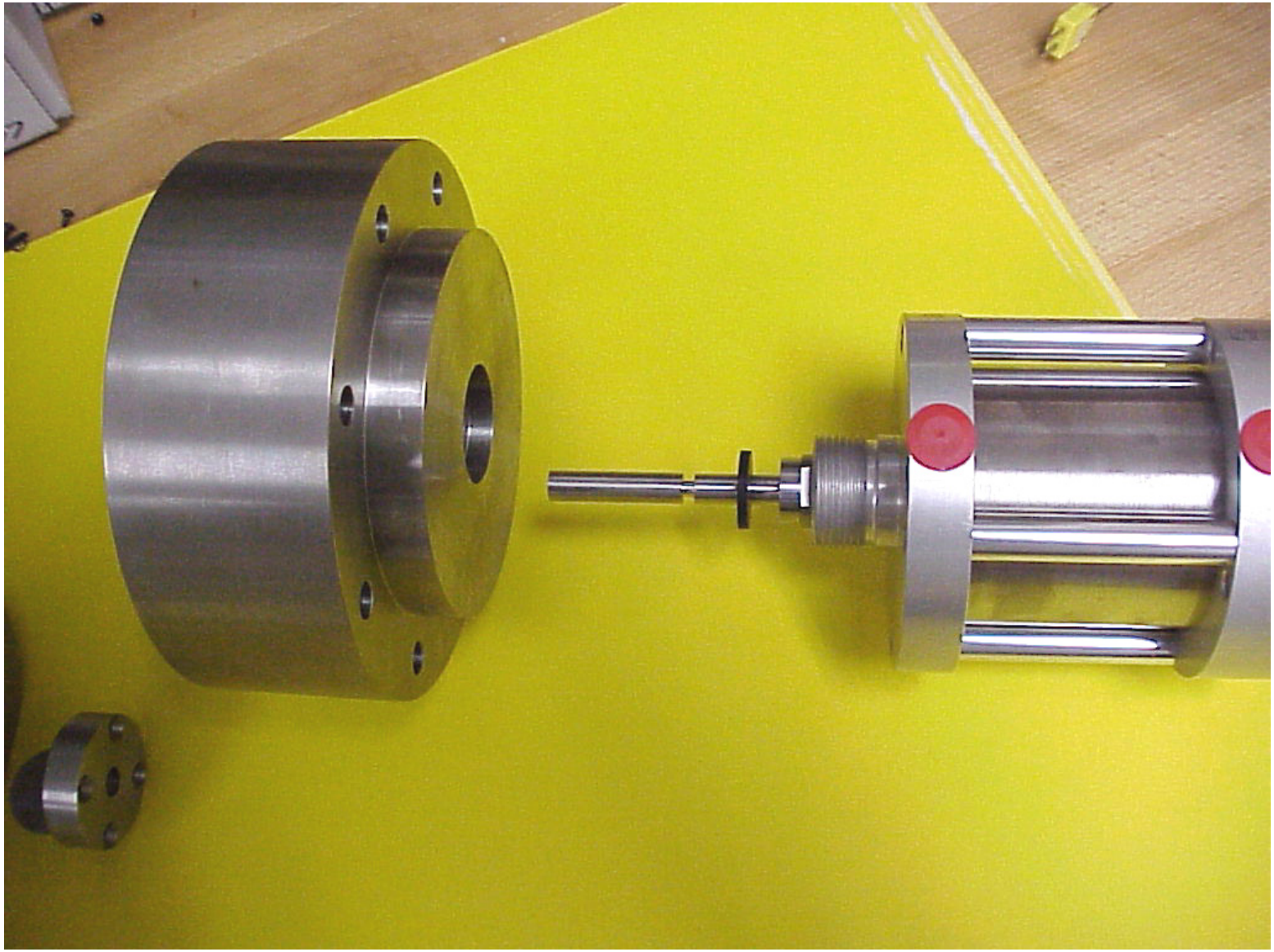

Figure 6. Plunger unit

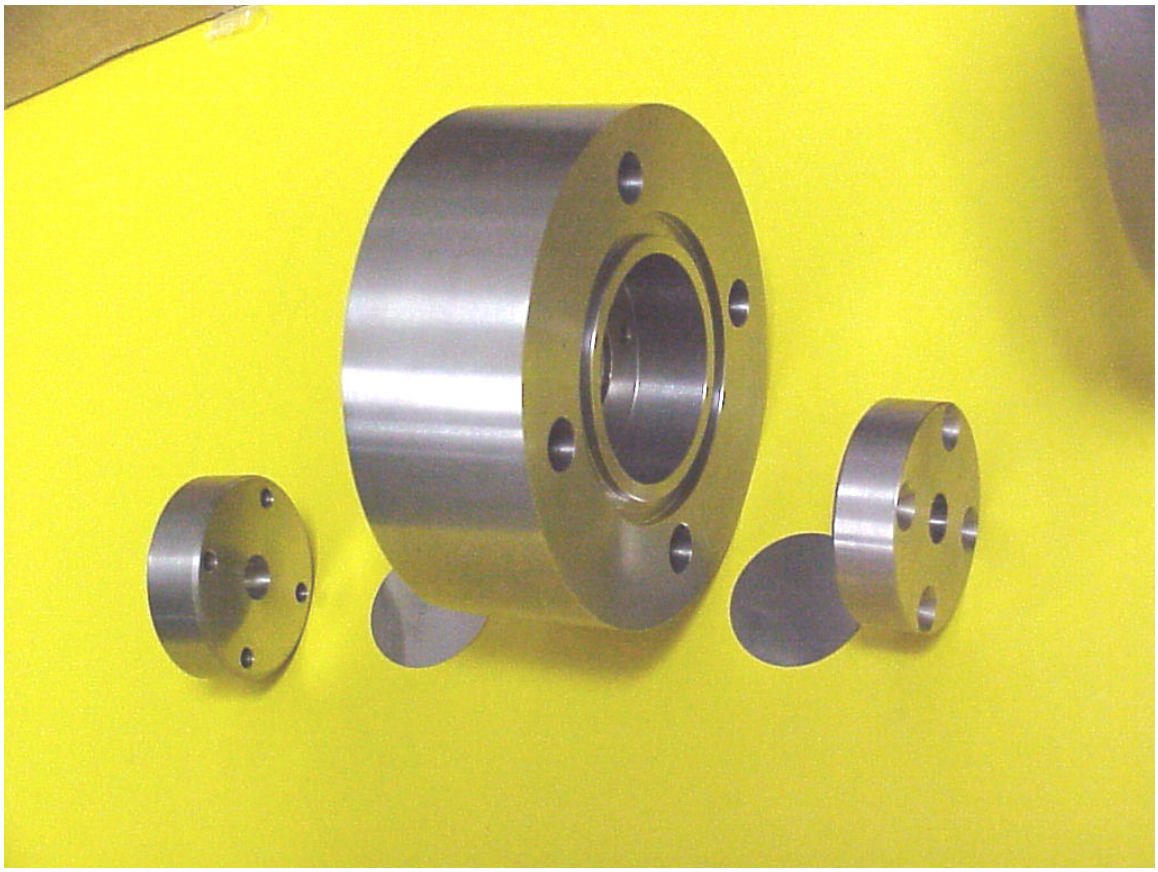

Figure 7. Pellet section

Energetic Material Evaluation

The original project concept held an expectation that cesium or related metals would, when put in contact with water in the fractures, react vigorously and supply sufficient heat to vaporize the water and generate a steam explosion. However, testing in the previously described test chamber showed that the pressure pulse generated by such a reaction was insufficient for project parameters (too slow).

The poor reactions of group 1 and 2 alkali and alkaline earth metals set off a search for other materials that could function properly. Materials that were examined included lithium aluminum hydride, sodium hydride, lithium borohydride, aluminum and beryllium borohydrides, the sodium salt of nitromethane and barium carbide. These all produced violent reactions, but with insufficient energy or poor reliability. The reactive oxidizer sodium peroxide was tested with the metal fuel magnesium, and then with the organic fuel hexamethylene tetramine, but drop tests of water on appropriate material mixtures gave generally disappointing results, contrary to literature.

Material selection has been performed primarily using the drop test. In this test, a small amount of the candidate mixture is placed in a tiny plastic beaker, and a drop of water remotely added with an automatic pipette. The reaction of the test material is monitored and assessed. Promising mixtures are then subjected to a capsule test, where a small quantity of mixture is placed in a small capsule with a pinhole in the end. The capsule is dropped into a large container of water, and the reaction observed. The water ingress is slowed with a water permeable barrier at the pinhole. Materials that are found to be possible candidates are then tested in the test chamber so that the pulse rise time and shape can be measured. This

information is critical for modeling of the waveform characteristics, attenuation, and other parameters necessary for assuring that the pulse is optimal for detection.

The original test chamber was also modified for ease of use and for application in the lab instead of a test cell. In addition, finite element analyses were performed to assess maximum pressure and temperature conditions that can be applied to the chamber due to detonation of the charge.

In testing several other combinations of materials, two reactions were discovered that appear to be more than sufficient for these purposes. These include the reaction of silver nitrate and magnesium upon contact with water and ceric ammonium nitrate and magnesium upon contact with water. Both reactions were investigated at length and found to show prompt and reliable vigorous activity that is more than sufficient to fire an explosive component and possibly are sufficiently energetic alone that an explosive component may not be required. Silver nitrate and magnesium, for example, react in a two-stage manner. Initially, water promotes an electrochemical exchange between the silver ion and the magnesium metal; the magnesium donates electrons to the silver, reducing the silver, while the silver oxidizes the magnesium. The heat generated in this electrochemical exchange then initiates the pyrochemical reaction whereby the nitrate anion of the silver decomposes and the oxygen burns the magnesium.

Given the success with silver nitrate and magnesium, an effort was also made to find other similar reactions that would require less expensive materials (silver nitrate is relatively expensive). Iron and chromium nitrates, ruthenium chloride and copper chloride were tried, but results were not as successful. Ceric ammonium nitrate is the one other possibility that has promise, but there may be some other hazards associated with it and additional characterization would be required (thus, no further evaluation was attempted).

Since the change of focus from an alkali metal reaction to a pyrotechnic initiation mixture that may be activated by fracture fluid, the focus of development has been on characterizing that ignition mixture. There exists a variety of possibilities for the ignition composition, which includes silver nitrate with magnesium, silver nitrate with magnalium, and ceric ammonium nitrate with magnesium. All three mixtures function with a similar mechanism. Because of the fact that silver nitrate/magnesium is a relatively unknown mixture, it is important to define the properties of the mixture. Also, the silver nitrate with magnalium, and ceric ammonium nitrate with magnesium are novel mixtures for which no data is available whatsoever. The mixtures are under evaluation to quantify their operational limits.

The ceric ammonium nitrate mixture has been eliminated based on the low decomposition temperature of the ceric ammonium nitrate, and the hygroscopic nature of that oxidizer. The silver nitrate with magnalium mixture held promise for possible handling advantages of an aluminum/magnesium alloy over pure magnesium. The Differential Scanning Calorimetry data, however, point to the silver nitrate with magnesium as the logical choice since it ignites in the region of 170 ^{o}C, as shown in Figure 8, and its reaction is nearly complete at this point. It was hoped that the magnalium mixture would give a higher ignition temperature, and that it would be correspondingly safer to handle, mix, and store. Unfortunately, as shown in Figure 9, the magnalium mixture ignites at a similar temperature, of about 167 ^{o}C and the reaction is not as complete as the reaction with magnesium.

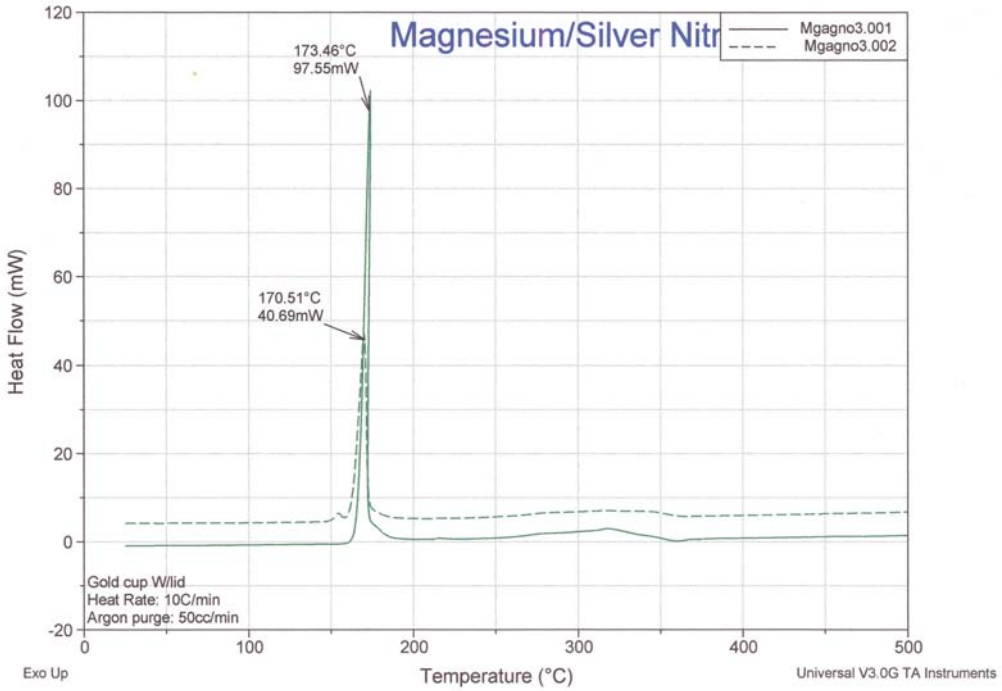

Figure 8. Magnesium/Silver Nitrate mixture behavior.

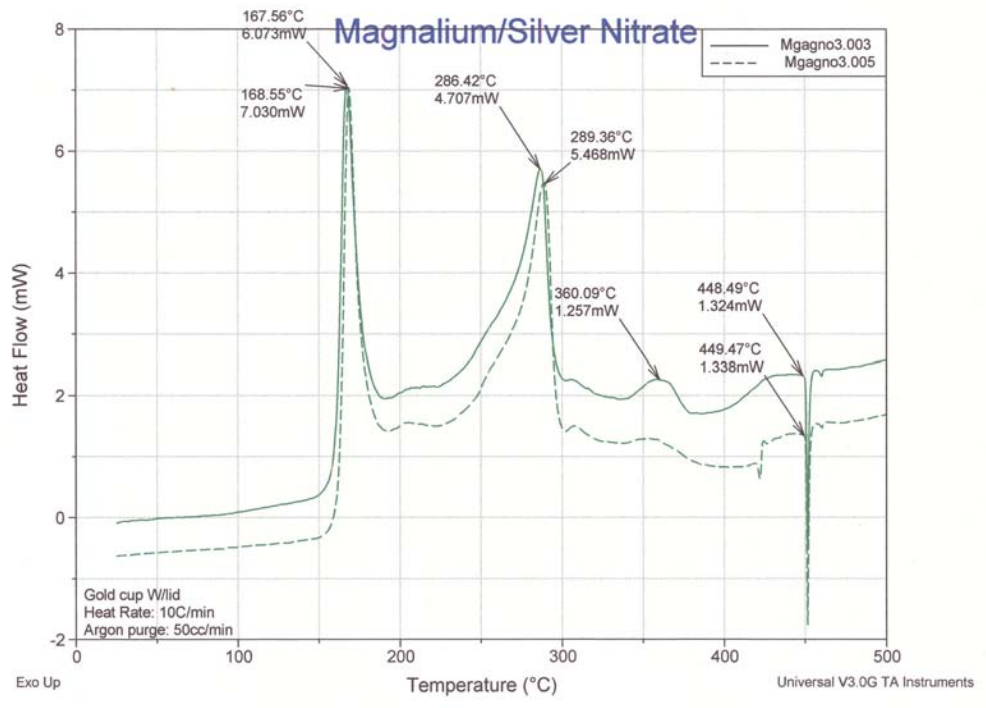

Figure 9. Magnalium/Silver Nitrate mixture behavior.

Other possibilities were explored to find a more stable mixture, with findings that again point to the silver nitrate with magnesium mixture. For a variety of reasons, other possible nitrates are unsuitable. Many of the transition metal nitrates are very hygroscopic, decompose at relatively low temperatures, or are not available pure. Based on electrical potentials, replacing the magnesium also seems unlikely.

Thus, the material system for initial evaluation has essentially been chosen. It consists of a silver nitrate and magnesium primer mix that will react with water to initiate an output charge (if necessary). BNCP has already been selected for the output charge (BNCP stands for bis-tetrazolatotetramminecobalt(III) perchlorate). BNCP was selected for its good energy output and its capability to detonate in a very short distance (it will work as a small particle). The particle size of the silver nitrate and the particle size and morphology of the magnesium can be varied to change reaction rates and for ease of handling and processing. Other components may also be added to the primer mix for a greater range of reaction variability.

Analysis of this system continued in order to finish characterization of the ignition mixture, as well as possible output charges. Accelerating Rate Calorimetry (ARC), an adiabatic calorimetry used for reactor and pilot plant safety analysis; was used to determine time, temperature, and pressure relationships for these exothermic reactions. Thermal and pressure hazard parameters related to ARC data include, onset temperature, adiabatic temperature rise, pressure generation rate, time to maximum rate, temperature of no return, and self accelerating decomposition temperature. To understand the effects of heat soak, high temperature storage, and in particular aging, isothermal long-term aging tests were conducted to observe any adverse effects that aging had upon the mixture/components. In these tests, a sample is held at a constant elevated temperature for a period of time, and then analyzed. A specific friction test, called the BAM test, can also be performed. In this test, a porcelain pin is slid on a line of composition, which is resting on a porcelain plate. The pin and plate are constants, as is the speed of the pin on the plate surface. The variable is the force with which the pin is held against the plate. This test gives a reproducible number for the sensitivity, which can then allow the sensitivity of the mixture to be related to known compounds which will allow proper precautions to be taken for safe handling. Also a handling test, the ESD, or electrostatic discharge test, uses a charged capacitor to simulate a stray static spark jumping into the composition. Charging the capacitor more or less before allowing a pin to approach the composition and discharge, will vary the energy of the spark. Similar to the BAM friction test, the sensitivity is placed within a framework of known compounds and mixtures, so that appropriate levels of precaution can be recommended.

In order to provide further characterization of the energetic materials, a Henkin tester was constructed to evaluate the time for the materials to cook off at temperature. This is critical information for designing the particles for use under varying depth conditions (higher temperature and pressure). The Henkin test apparatus, shown in Figure 10, gives time-to-explosion for these mixtures as a function of temperature. The time-to-explosion shows any change in thermal stability caused by the addition of other chemicals or compounds. By this test, compatibility issues may be addressed at the design and formulation stage.

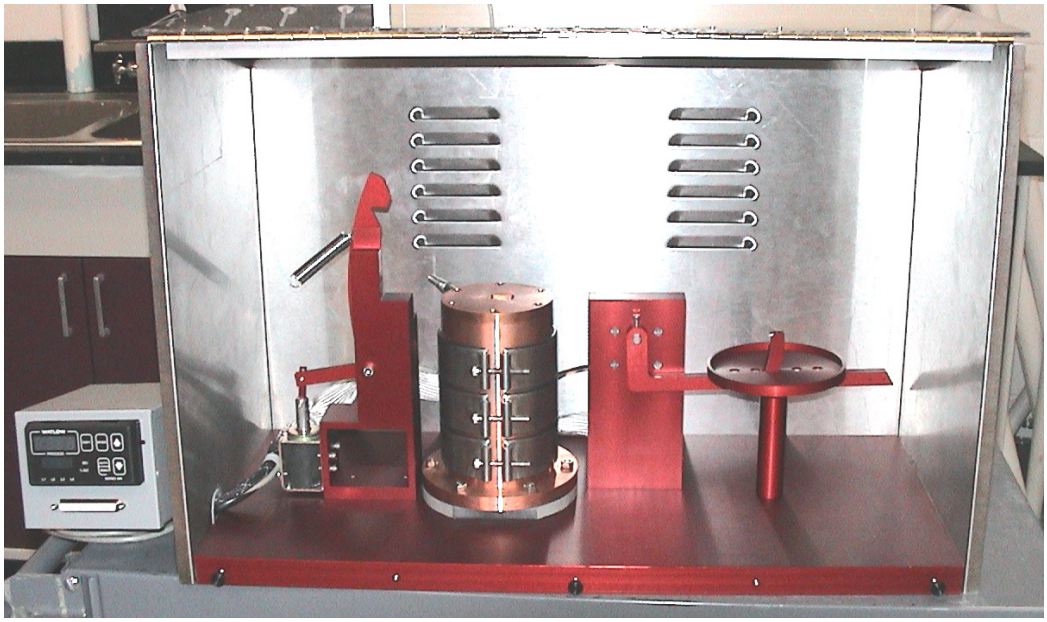

Figure 10. Henkin test apparatus.

There are other tests to perform, such as confirming the ability of the ignition mix to react with the fracture fluid, and choosing the correct corrodible or dissolving plug to act as a "time fuse." For these tests, actual fracture fluid is used to simulate most closely the deep well environment.

Triggering Systems

The triggering process work has taken place along two separate approaches. The simple approach has been to design a case with a corrodible plug. The corrosion plug is designed to so that it has an appropriate "safe time" based upon fracturing conditions and other parameters (typically a couple of hours). This plug design is relatively straightforward and depends primarily on the material that will react with the water, so efforts have concentrated on more elaborate designs.

The more sophisticated triggering process involves the use of a micro SCB (semiconductor bridge). In this design, some power source (battery or capacitor) powers a timer to fire the SCB. Work in this area has proceeded along three lines. Most of the activity has focused on developing a micro SCB that could function with a low power source; other work has been to find and test low-power-source timers and evaluate both capacitors and batteries for the internal power requirements.

Semiconductor Bridges (SCB) for Low Energy Ignition of Acoustic Explosive Pellets

Semiconductor bridges (SCB) are ignition devices that produce DC gas plasma that effectively initiates energetic materials. These devices can be sized to require only 10's of millijoules for initiation. The basic idea underlying an SCB is that semiconductors decrease their resistance as they get hotter, while metal resistance increases as they are heated. SCBs have been made in two different ways: as a pure, highly doped silicon or as a sandwich of silicon and a metal, such as tungsten (W). In the latter case, the metal initially conducts most of the current, but as it heats, gradually transfers the current to the silicon. The silicon melts, then boils and forms a gas plasma. The electron temperature in this plasma is several million degrees C. This device usually requires 10 millijoules or more to ignite. The silicon plasma continues to conduct current and ignites the energetic material.

Device Selection/Development

Due to size constraints, the micro-firing circuit used to initiate the bridge had both a low voltage potential (13 volts) and limited stored energy (20μJ). In many firing circuits, voltage potential and available energy are typically not an issue. To guarantee that a well-characterized SCB will initiate, an increase in the firing voltage might be all that is needed. In some cases a device may require more energy to sustain a plasma large enough to ignite an energetic material. To ensure that the plasma energy is sufficient, more stored energy in the form of added parallel capacitance would be provided. In this application, it was important to identify a device that would efficiently utilize the available voltage and stored energy resources. The primary objective was to determine the maximum bridge volume that could be successfully initiated within the firing circuit limitations. Although not proven in this series of test, it is suspected that bridge volume directly impacts an SCB's ability to initiate an energetic material. A higher bridge volume has a better chance of igniting an energetic material than a lower bridge volume. A mask was designed to explore various bridge volumes and dimensions. Table 1 shows a detailed matrix of devices designed for testing.

Table 1. SCB devices designed for testing

L (μm)	W (μm)	D (μm)	*V (μm^3)	Type	**Rs (ohm)	Bridge R (ohms)	***Total R (ohms)
611	125	1	76375	Pd-Si	0.163	0.80	1.00
489	100	1	48900	Pd/Si	0.163	0.80	1.00
175	**30**	**1**	**5250**	**Pd/Si**	**0.163**	**0.95**	**1.15**
150	30	1	4500	Pd/Si	0.163	0.82	1.02
125	30	1	3750	Pd/Si	0.163	0.68	0.88
10	**30**	**1**	**600**	**Pd/Si x2**	**0.163**	**0.2**	**0.8**
75	15	1	1125	Pd/Si	0.163	0.82	1.02
10	**30**	**1**	**300**	**Pd/Si**	**0.163**	**0.2**	**0.4**
100	380	2	76000	n-phos Si	3.5	0.92	1.12
90	**270**	**2**	**48600**	**n-phos Si**	**3.5**	**1.17**	**1.37**
32	**80**	**2**	**5120**	**n-phos Si**	**3.5**	**1.40**	**1.60**
23	80	2	3680	n-phos Si	3.5	1.01	1.21
8	80	2	1280	n-phos Si	3.5	0.35	0.55
16	40	2	1280	n-phos Si	3.5	1.40	1.60
15	36	2	1080	n-phos Si	3.5	1.46	1.66
11.5	40	2	920	n-phos Si	3.5	1.01	1.21
8	40	2	640	n-phos Si	3.5	0.70	0.90
4	40	2	320	n-phos Si	3.5	0.35	0.55

*Volume represents the total Si volume in the bridge area.

** Sheet resistance of the material in the exposed bridge area.

***Total R includes the device resistance plus package resistance.

A group of H-Pattern, 300-μm^3 Pd-Si devices were first fabricated and tested. Initial measurements indicate that the bridge resistance of 0.2-ohms was consistent with design expectations. The addition of a TO-46 package with wire bonds increases the overall packaged device resistance to 0.4-ohms. In the first series of tests, the Pd-Si device provided positive results. Although this device has a fast initiation time of less than 1 microsecond, the maximum bridge volume that could be completely fired is limited to about 600-μm^3. Shown in Figure 11, is a 300-μm^3, 0.4-ohm device. The residue in the area surrounding the bridge indicates that the bridge material sufficiently vaporizes and then re-deposits as plasma energy drops.

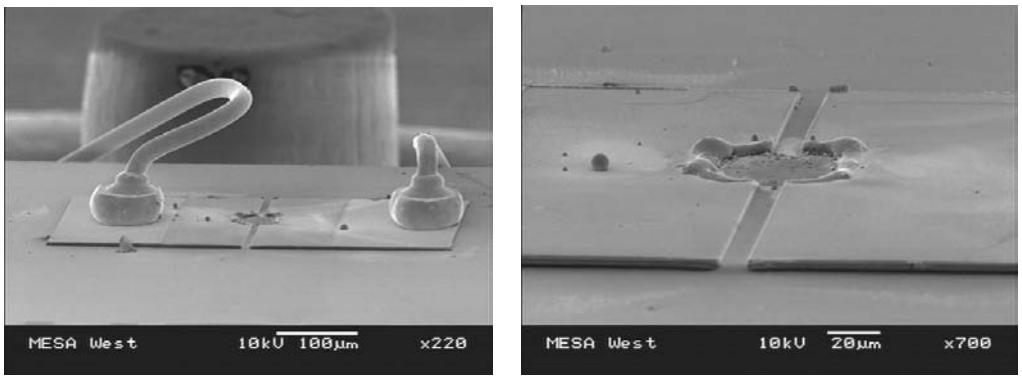

Figure 11. 300-μm^3 Pd-Si SCB.

A problem with low resistance bridges is that the firing circuit and package resistance become an appreciable part of overall circuit resistance. In its most basic form, the circuit between the energy storage device (capacitor) and bridge resembles a series resistive circuit. Therefore, the applied voltage is divided between each of the components within the circuit. The total circuit resistance including a 0.2-ohm bridge is approximately 0.4 to 0.6-ohms. With a maximum firing voltage of 13-volts, having over one-third of this potential lost in the conductors presents a problem. Due to these circuit losses, the voltage supplied to the 0.2-ohm bridge is only about 4-volts. Because voltage potential is a key factor in maximizing the device's firing ability, circuit losses have to be controlled. In a firing circuit configuration where resources are not limited, simply increasing supply voltage by a factor of three would compensate for the losses in the conductors. To further increase the bridge volume without increasing firing voltage, circuit losses need to be minimized and/or the bridge resistance increased. It was determined that the best course of action would be to increase the device resistance to approximately 1-ohm. It is important to note that maintaining a low bridge resistance also enhances device stability by keeping at a low resistance above ground potential.

To meet the 1-ohm requirement with current 300-μm^3 devices, the total device resistance needed to increase by a factor of two. To accomplish this requirement quantity two, 300-μm^3, 0.4-ohm devices are placed into a series configuration. In a series circuit, the total resistance is the sum of the all the devices in series. Although the voltage drop across each device does not change in this configuration, the voltage drop across the two devices does increases by a factor of two. Therefore the voltage drop across each device is maintained at 4-volts with a total bridge area of 600-μm^3. There are a few potential problems with placing multiple devices in a series configuration. In an ideal scenario, both bridges would have an equivalent resistance. If the bridge resistances are equal, the voltage drop across each device is the same. However if one bridge has a higher or lower resistance than the other, the voltage drop across each independent bridge would become unbalanced. This imbalance could result in a fire, no-fire scenario for one or both devices. Another problem involves device reliability. Two devices placed in series require a jumper wire between the devices to complete the circuit. This jumper wire not only adds a small amount of series resistance, it also adds two additional contacts increasing the potential for device failure. A device could be designed to combine both bridges on one die using a simple metal interconnect the two devices together. Although this was considered, another concern arises with relation to distributed bridge volume. It is unknown if a dual point ignition source created by separated bridges would enhance or reduce a device's ability to initiate an energetic material. This could be another area worth investigating; however there are single bridge options that would better serve the low voltage, low energy firing circuit's needs.

Two separate dual SCB firing tests were performed. In both tests, the devices fired producing a bright flash. Inspection of devices following the first test shows that both devices appeared to have equivalent damage. In the second test shown in Figure 12, only one of the two series devices appears to completely fire. The amount of silicon re-deposited in the bridge area is considerably less than the single 0.4-ohm device shown in Figure 11. This could be an indication that the dual configuration is at its lower firing limit, or the result of a voltage imbalance due to improperly matched devices.

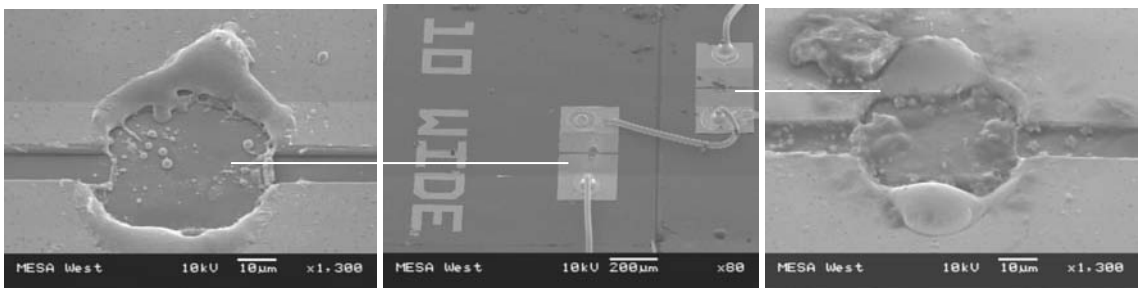

Figure 12. Dual 300 -µm^3 Series Pd-Si SCB.

To produce a single-bridge 1-ohm device, a redesign of the basic device was required. In an attempt to further simplify device design and improve device efficiency, a new source of highly doped n-type (phosphorus) silicon was found. This highly conductive silicon film allows a single layer 1-ohm device to be made eliminating the need for a parallel heating element (Pd or Si). The phosphorus doped Si exhibits both the phosphorus resistive properties at room temperature and the Si resistive properties at an elevated temperature. The 1-ohm devices are designed to maintain a 1-ohm total resistance, which includes the package and wire bond resistance. In order to meet this requirement, the bridges were designed for a target resistance of 0.8-ohms. With the new 0.8-ohm bridge resistance, the voltage supplied to the bridge would increase by a factor of two over the 0.2-ohm device.

The new group of devices fabricated out of n-phos Si was tested. Initial measurements indicate that the bridge resistance range from 0.8 ohms to 1.4 ohms is well within expectations. Figure 13 shows a 1.4-ohm, 5,120-µm^3 n-phos Si SCB after testing. A large portion of the bridge completely vaporizes and the material re-deposits around the bridge area. Note the amount of re-deposited Si and compare it to the single and dual 300-µm^3 devices shown in Figures 11 and 12. The amount of silicon and phosphorus re-deposited in the bridge area appears to be greater than the single and dual 0.4-ohm Pd-Si devices.

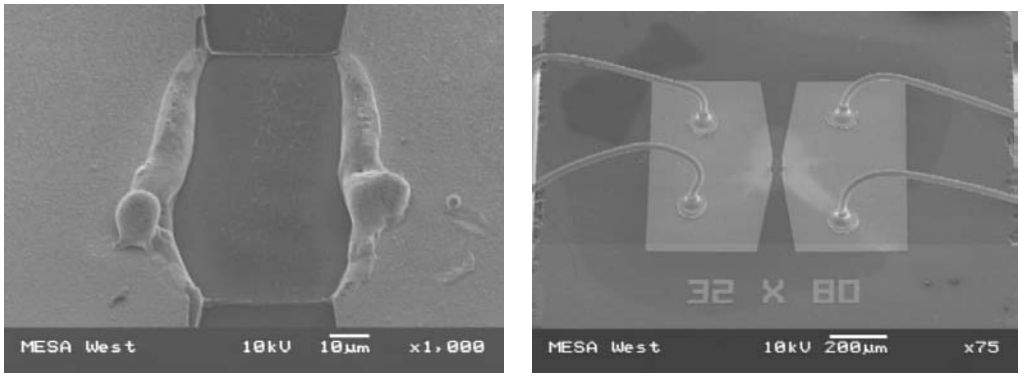

Figure 13. 5,120-µm^3 n-phos SCB.

If the n-phos Si bridge volume is too large and potential voltage is not sufficient, only a portion, if any, of the bridge volume vaporizes. In this scenario, additional stored energy (capacitance) would not provide any useful function. If the potential voltage were not large enough to sufficiently ignite the plasma, stored energy and material volume would not be completely utilized. An example of an insufficiently fired 48,600-µm^3 device is shown in Figure 14. As can be seen, the silicon appears to melt and not vaporize. The amount of re-deposited material around the bridge is considerably less. This would support the theory that voltage potential is key to initiating the plasma. If insufficient voltage were

applied to the bridge, the bridge material would simply act as a heater. Heat formed at the bridge would melt the material and then the heat would quickly dissipate into the substrate.

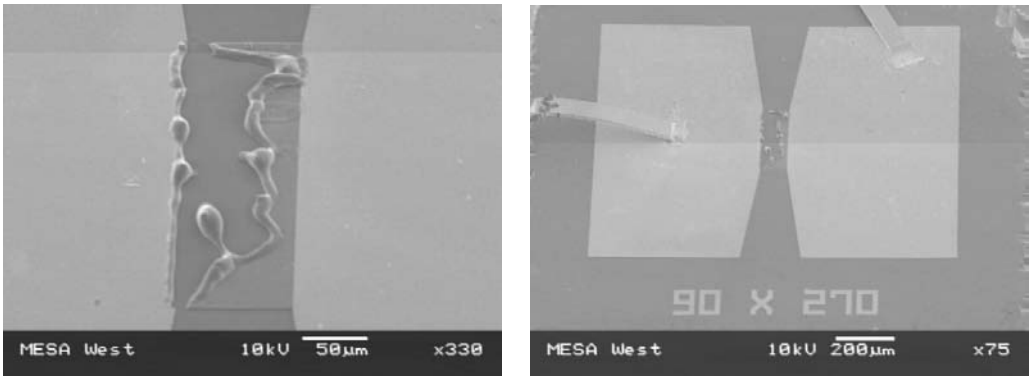

Figure 14. 48,600-µm^3 n-phos Si.

A few 1-ohm Pd-Si (single) devices were also tested. To develop a 1-ohm resistance, the bridge length had to be a multiple (4.8 times) of the bridge width. This reduction in the bridge's cross sectional area appears to reduce the current carrying capacity of the device. Similar to what is shown in Figure 14, the Pd would open the circuit before the silicon would sufficiently heat. The 5,250-µm^3 Pd-Si device was unable to fire at the N-Phos Si equivalent volume of 5,120-µm^3. So because of this, there was no need to continue testing the 1-ohm Pd-Si devices.

Figure 15 shows the progression in designs beginning with the 300-µm^3 device leading up the largest 48,600-µm^3 device. The largest volume device that successfully fired with the micro firing set was the 1.4-ohm, 5,120 µm^3 n-phos Si.

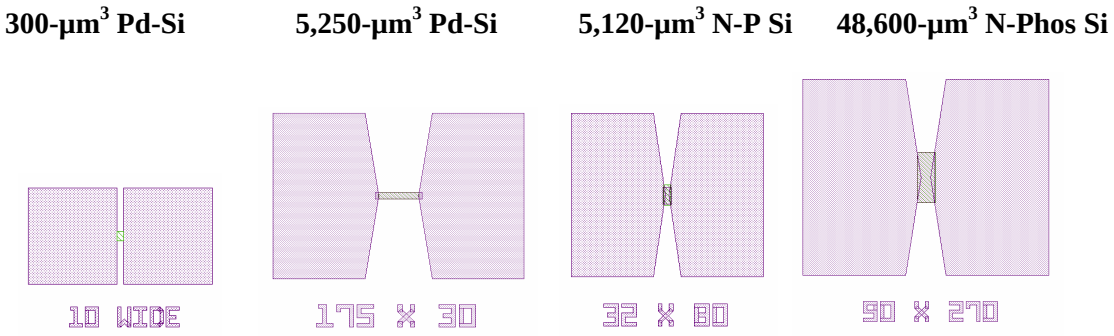

Figure 15 – SCB Design Variations.

The micro firing circuit and 5,120-µm^3 bridge combination was not tested with an energetic material. Although the two components appear to work well together, it is not known whether or not the small bridge volume would sufficiently initiate an energetic material. An independent test on a similar n-phos Si device with larger firing set configuration was conducted. With an energetic material packed against 48,600-µm^3 and 76,000-µm^3 devices, initiation of the energetic material occurred. It is important to note that in this independent test, a higher firing voltage (up to 50-volts) was used. Although it is possible for

lower bridge volumes to initiate higher sensitivity energetic materials, it is not clear whether or not the device would be stable. Further research would have to be conducted to determine the best energetic material to use for low volume, low voltage SCBs.

Pd-Si Device Process Flow

With almost half the number of layers required to fabricate a W-Si device, the Pd-Si device is less prone to defects and processing issues. Most of the metallization concerns are resolved with a single step metal evaporation-deposition. All of the metal layers used in the fabrication of the Pd-Si device are evaporated simultaneously without breaking vacuum. Maintaining vacuum provides the best possible condition for maximizing metal adhesion, minimizing layer-to-layer contact resistance and improving device efficiency. The Pd provides a similar function as the W without the need for an additional diffusion barrier layer or processing complexity.

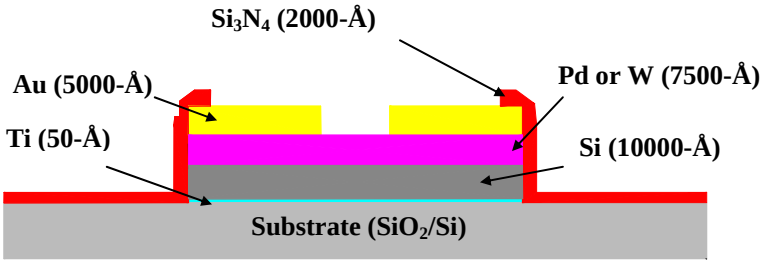

Figure 16. Pd-Si device.

Figure 16 shows a layer-by-layer breakdown of the current Pd-Si bridge design. Similar to the W-Si design, the substrate material consists of standard Si with 1-µm of thermally grown silicon dioxide (SiO_2) as an isolation layer. To prepare the SiO_2 surface for processing, the substrate must go through Piranha (3-sulfuric acid: 1-hydrogen peroxide) and dilute BOE (6-hydrofluoric acid: 1-ammonium fluoride: 100-DI water) acid cleaning steps. After thorough rinsing, the substrate must be dehydration baked for several minutes to prepare for photolithography. The Pd-Si device uses standard lift-off photolithography processes using a negative photoresist. A typical photolithography process includes surface treatment with hexamethyldisilazane (HMDS), resist dispense/spin, soft bake, exposure, post exposure bake, and then develop. When photoresist develop is complete, open areas will receive a metal deposition while areas protected with photoresist will not. The substrate goes through an oxygen (O_2) plasma clean to remove any organic scum that might reside on the substrate surface.

Before depositing titanium (Ti), the exposed SiO_2 surface is ion milled to remove surface contaminants that might inhibit metal adhesion. Immediately following ion mill, without breaking vacuum 50-Å of Ti, 1.0-µm of Poly-Si, 7500-Å of Pd, and 5000-Å of Gold (Au) are e-beam evaporated onto the exposed substrate surface. Ti with its reactive properties cleans and further enhances the bond between the SiO_2 and Si creating a strong foundation for subsequent metal layers.

Following e-beam metal evaporation of the Ti-Si-Pd-Au, the substrate is submerged in acetone. Acetone dissolves the photoresist and lifts unwanted metal from the substrate surface retaining the desired pattern. Substrate is final rinsed in DI water before receiving a 2000-Å PECVD silicon nitride (Si_3N_4) deposition. After Si_3N_4 deposition, the device is patterned using standard photolithography techniques.
The bridge and pads are exposed by etching the Si_3N_4 with 10:1 carbon tetrafluoride (CF_4):O_2 etch in a Reactive Ion Etcher (RIE).

To expose the Pd bridge, the substrate is patterned for Au etch using positive resist and standard photolithography techniques. In the Au etch step, the top 5000Å of Au positioned over the bridge is removed with a tri-iodide (80-g potassium iodide: 20-g iodine: 800-ml DI H_2O) solution. After Au etch, the substrate is goes through a series of solvent cleans to dissolve residual iodine and photoresist. The completed SCB goes through a series of steps that include e-test, dicing, cleaning, and packaging.

n-phos Si Device Process Flow

Requiring only two metal/semi-metal layers, the n-phos Si SCB is probably the least complicated of the three devices to fabricate. Using SOI (Silicon On Insulator) technology, the 2-µm top layer of poly-Si is heavily doped with phosphorus (P) to lower the film resistance. A Cr-Au metal layer above the poly-Si with Si_3N_4 dielectric is all that is required to complete the device.

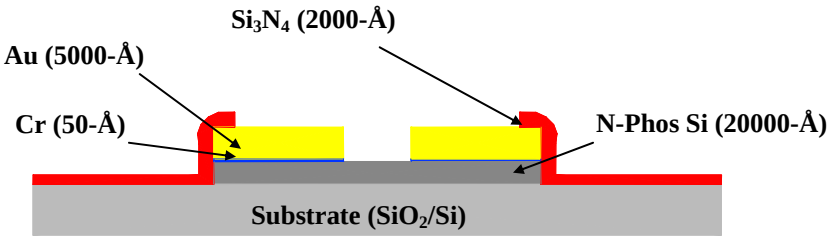

Figure 17. n-phos Si SCB device.

Figure 17 shows a layer-by-layer breakdown of the current N-Phos Si bridge design. Starting material consists of phosphorus-doped poly-Si on top of 0.75-µm thermally grown SiO_2. To prepare for metal deposition the SOI substrate must go through Piranha and dilute BOE acid cleaning steps. After a thorough rinse of the substrate, in preparation for photolithography the substrate must be dehydration baked. Using a negative resist, the n-phos Si device uses the same lift-off photolithography process as the Si-Pd device. After develop and rinse, to remove any scum that might remain on the substrate surface, the substrate goes through an O_2 plasma clean.

Before the substrate is loaded into an evaporator, the substrate is dipped in a dilute BOE to remove any oxides that may have formed on the surface of the Si. Before depositing Cr-Au, the n-phos Si surface is ion milled. Immediately following ion mill, 50-Å of Cr followed by 5000-Å of Au is E-Beam evaporated onto the doped poly-Si surface. Cr similar to Ti acts as an adhesion promoter to enhance the bond between the Poly-Si and Au. Because Cr does not appear to diffuse as easily into the Au as Ti, it is used as the adhesion layer.

Following e-beam evaporation of the Cr-Au, the substrate is submerged in acetone for removal of unwanted metal. The substrate is final rinsed with DI water before receiving a 2000-Å PECVD Si_3N_4 deposition. After the Si_3N_4 dielectric deposition, the device is patterned then reactive ion etched to expose the bridge and pads.

To expose the n-phos Si bridge, the substrate is patterned using standard photolithography techniques for Au etch. In the Au etch step, the top 5000-Å of Au positioned over the bridge is removed in potassium iodide/iodine solution. After Au etch, the substrate quickly goes through a series of solvent cleans to

dissolve residual iodine and photoresist. Following rinse, the substrate is quickly dipped in Cr-7 a chromium etchant and then rinsed with DI water.

The completed SCB device goes through a series of steps that include e-test, dicing, cleaning, and packaging before delivery to the end user. In some cases, during e-test a higher than normal bridge resistance is measured. It is believed that this elevation in device resistance is due to a high interlayer contact resistance at the Au and n-phos Si interface. To improve contact resistance at this interface, the completed device must be N_2 annealed at 420°C for 15s. Extreme care must be taken during the annealing operation to prevent device damage. One observation showed that the device resistance increases if the annealing process is too long. Another extended anneal resulted in Si_3N_4 failure and de-lamination.

MicroExplosives Electronics Development

The goal of this task was to develop a small timer/energy source capable of "firing" a micro size/ low voltage SCB. These newer micro versions of SCB's are now available and the goal was to determine what would be required to "fire" a micro SCB with the lowest possible voltage thus enabling reduced electronics size and ultimately a very small overall package.

To this end several electrical designs were produced. The first was based on a simple timer chip with limited flexibility while the second was built using an 8-pin micro-controller, which would allow for a variety of timing/firing combinations to support various project requirements. Both "fire sets" were built using a low resistance field-effect transistor (FET) as the trigger switch. Figure 18 shows the overall circuit of the second design. The circuit consists of 3 basic pieces (4 if you include a specific trigger generation circuit): the control element (U1), the voltage generator (U2) and the energy handler (storage (C3) and switch (FET)). The control element consists of a PIC microcontroller (U1), which determines when to start timing, when to turn on the voltage generator and when to fire the SCB. The processor makes a good control element (vs. programmable logic) because it is easy to adjust all the parameters and it is a very low power component.

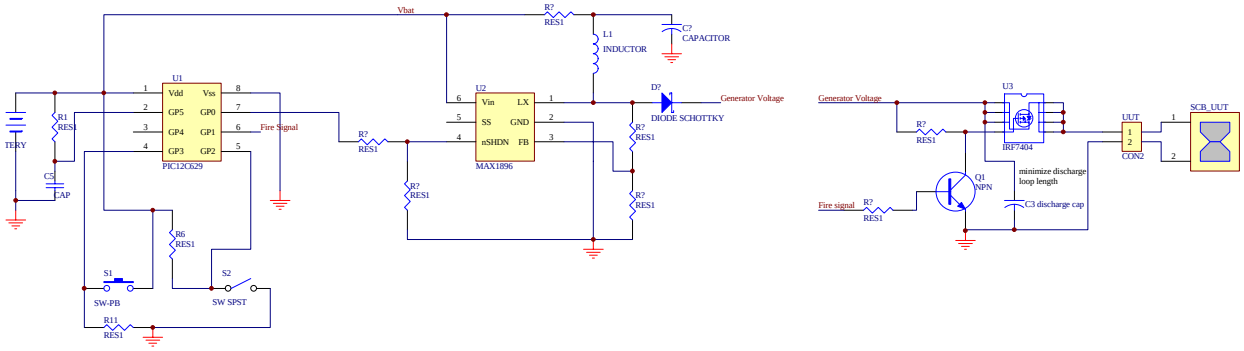

Figure 18. Schematic of complete circuit.

The basic operation of the circuit is for the controller to start timing based on an input transition (in our test case a simple trigger switch) from a triggering source. After receiving a trigger the processor would measure time for a predetermined interval, turn on the voltage generator then fire the SCB. The following sections will be discussed; triggering, timing, voltage generation and the firing circuit.

Triggering

The trigger source could be a simple switch (S1 used for our testing) or a number of alternate trigger options, which would depend on the end use. An inductive trigger circuit was developed for the first circuit, which would initiate a trigger based on inductive coupling from a trigger controller at a specific frequency and very close proximity. This would allow a unit to be triggered by passing the unit within the required distance of a trigger controller but with a low probability of false triggering due to the specific frequency. Any number of trigger inputs could be tied to the trigger pin of the microcontroller allowing for different trigger mechanisms based on use and safety. Some alternates might be; optical, coded optical, time on applied power, trigger on switch closure and numerous others. Trigger mechanisms were not specifically developed for this project and would depend on end use.

Timing

All aspects of timing and triggering are controlled by the microprocessor. The microprocessor can be programmed for a wide range of trigger-to-fire delays depending on use. The processor as it is used here can easily provide a timing range of 0 to years with the primary constraint being battery life. When used for testing the timing was set to zero in order to provide for proper scope triggering. The voltage generator however could be left on during firing or turned off prior to trigger.

Voltage Generation

Since the initial goal was to generate a “large” discharge voltage from a battery, some form of voltage boost circuit would be required. Since size reduction was also of interest there was a trade off between the sizes of all the components involved in the voltage generation process. With the advent of the latest generation of boost regulators for use in miniature systems, like cell phones, there were a number of commercial IC’s available for use in this application. We considered using the processor to drive a LC boost circuit but this would still require using a active device as the inductive switch and, given the size of the new IC’s, it turned out to be just as effective to use a commercial generator IC.

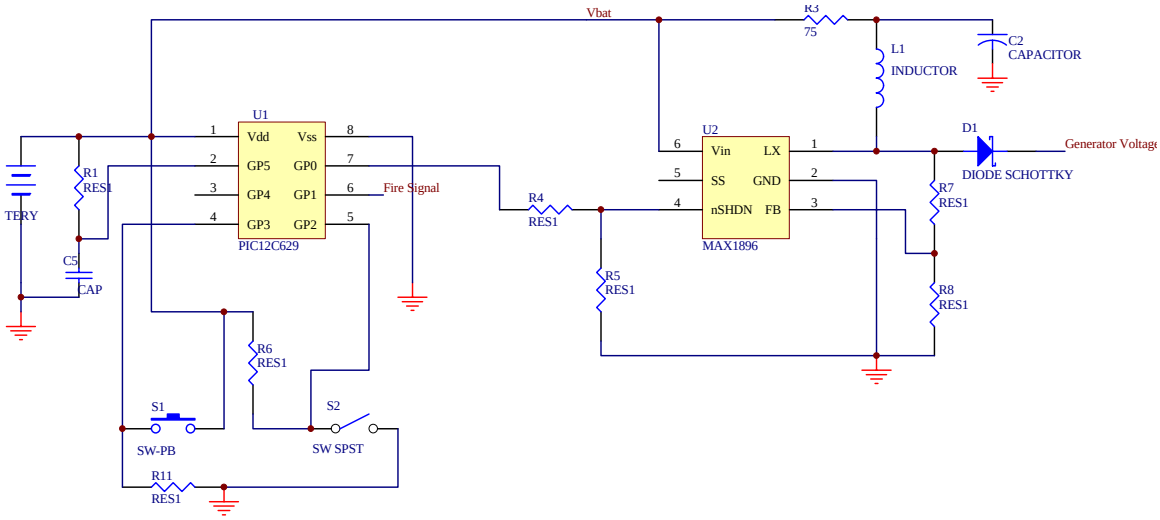

Figure 19 – timing and voltage generation.

The circuit consists of a boost regulator IC (in a tiny 6 pin SOT package labeled U2 in Figure 19), an inductor (L1), the switch diode, and the final charge storage capacitor. Because we did not initially know what voltage level a potential SCB might require we settled on the highest value available for this size generator (around 12v – 4x the 3 v battery input). In retrospect a higher voltage would probably be better (up to 20 v) but we have demonstrated firing several types of small SCB’s with the 12-v level. Figure 19 shows the schematic of the voltage generator, while the storage capacitor and firing switch are in

Figure 20. The Generator IC operates at 200 kHz and charges the storage capacitor (10-20 µF) in approx 200 msec. In operating from a battery only 2 or 3 charges of the storage capacitor are possible before the battery voltage is too low to operate the circuit, but in a real application only 1 is required.

The voltage generator is activated by a control line from the microprocessor. At the appropriate time the microprocessor pulls the generator control line high which allows the generator to charge the storage capacitor from the battery voltage to about 13 volts. The charging action takes about 100 msec. A series resistance R3 controls the maximum long term current available to the generator while a generator input capacitor (C2) allows the generator to produce the high input current used by the boost inductor. The series resistor also limits the maximum current which can be drawn from the small main battery thus controlling the drop in battery voltage during initial output cap charging (to the battery voltage) and during final voltage generation when the generation circuit is activated.

Firing Circuit

The last circuit to discuss is the firing circuit. The firing circuit (Figure 20) is composed of the storage capacitor (C3), the FET switch (IRF7404) the trigger control circuit (Q1) the SCB. A FET was chosen for the firing switch because of the very low on resistance, large number of types available, and a wide range of packaging. Several FET's were evaluated and all worked very well. The unit, which was used in the final testing, was a HEXFET from International Rectifier. It has an on resistance of about .04 ohms. Since our SCB's varied from .4 ohm to 4 ohms this FET was a good match. Some initial FET turn-on-timing problems occurred that were related to the control transistor drive currents. The turn-on time was improved by increasing the transistor drive current and by changing to a higher frequency device. Changing the control device to a FET would be a recommended for this circuit. Turn-on time is in the range of 200-400 nsec, which is more than adequate for this application but using a FET as the control element would require less drive current. The firing circuit control timing is determined by the microprocessor and can be programmed to any required value.

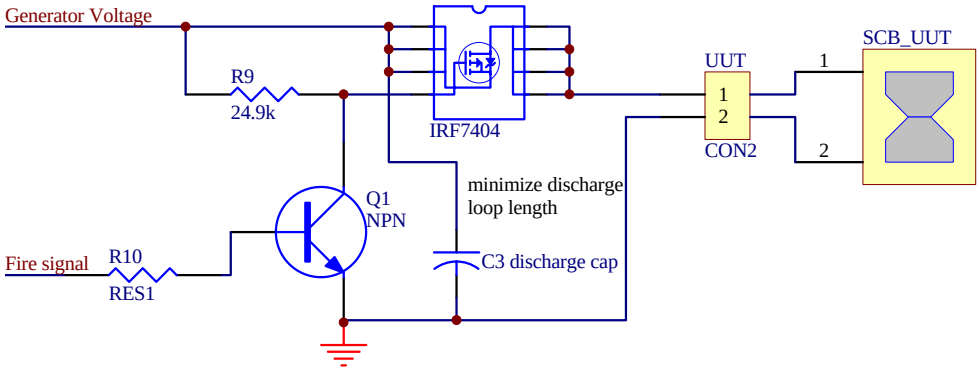

Figure 20. Firing circuit.

Figure 21 shows the circuit board as developed for testing. The battery holder would not be used in a final product and the components could be spaced closer and/or applied to both top and bottom of the board. Even with the use of standard commercial packaging the board size of a final product could be reduced to less than half the size used in the demo board (1.8"x1.2"). The battery will be the largest component on the board and will control the ultimate size of the system. Note that the microprocessor is in an 8-pin DIP package for testing but would be a SOP or smaller package in a final design.

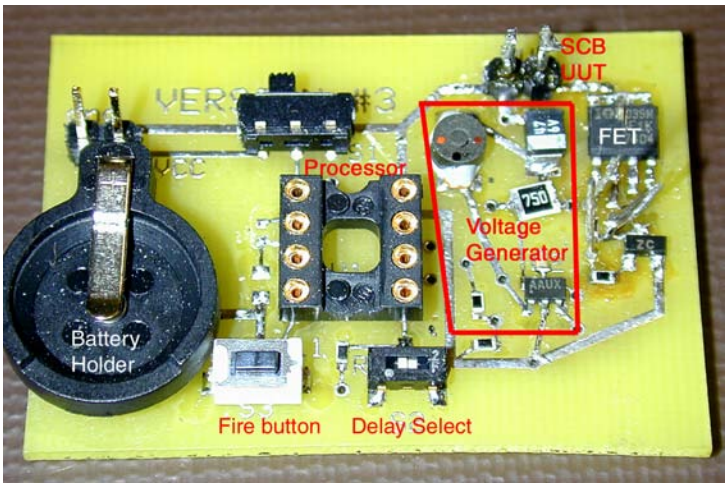

Figure 21. SCB Fire Set.

Testing

Testing started with a 0.4 ohm Pd-Si SCB. We were trying to get closer to 1 ohm but bridge design limitations produced 0.4-ohm devices. The initial tests proved that the circuit could fire the device. The device fired in about 1usec with energy in the range of 60uJ. Figure 22 shows the capacitor voltage and SCB voltage vs. time. As the voltage is applied to the SCB the resistance holds until high-energy interactions occur followed by the device opening (electrically) and the voltage coming back to the pre-fire level. During the high-energy interaction time the resistance is low enough to cause circuit voltage drops depending on various component internal resistances. Figure 22b shows the "fired" SCB.

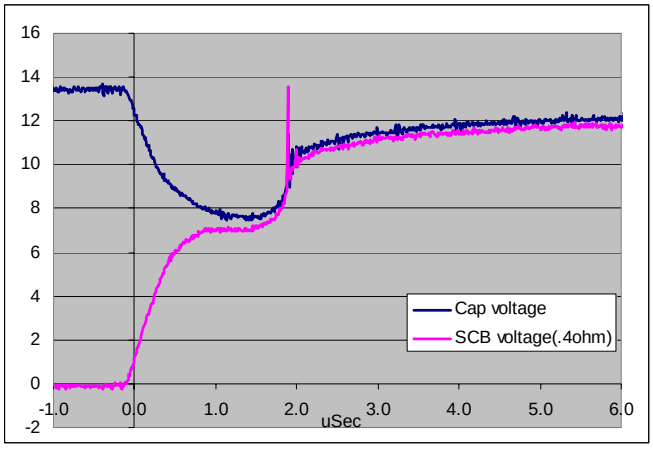

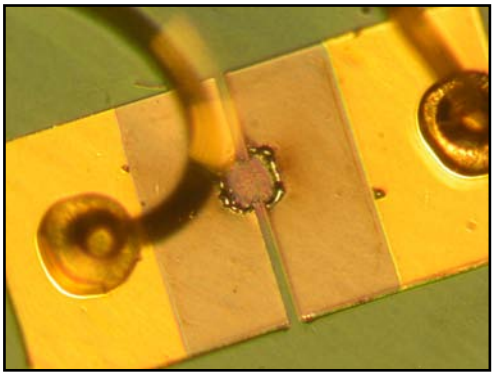

Figure 22. (a) 0.4 ohm Pd-Si SCB test; (b) "Fired" SCB.

During the 0.4 ohm testing the discharge FET control voltage was monitored and found to be the dominant rise time control. Additional testing was done to decrease the rise time by increasing the capacitance, using a lower inductance FET (L was not dominate and this did not help) and by increasing the drive to the control NPN transistor (dominate rise time mechanism). The control voltage is shown in Figure 23 and shows differences between the initial capacitor, double the capacitance value, and

increasing the drive current to the NPN control element. After this point all testing was done with 20 µF capacitance and higher drive current. The rise time evaluation was done using a 1-ohm resistive load.

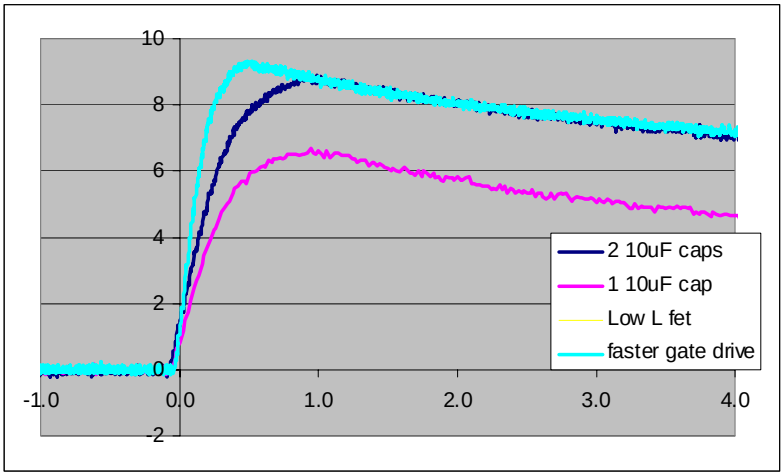

Figure 23. Rise time Improvements.

A number of SCB's were evaluated to determine whether the 12-v system had enough energy to fire them. Large devices could not be fired with 12-v, but devices in the medium size range were fired with 12-v. Several larger devices were fired using 20-v in a circuit configuration without the generator. The 20-v level was externally applied but still triggered by the microprocessor using the existing circuit. The 20-v level was the maximum allowed for discharge FET hence no testing was not done beyond 20-v. The problem with using 20-v in a final circuit is that a higher voltage boost generator is required and higher voltage capacitors would also be needed. Unfortunately raising the voltage makes the circuit grow in size, but increasing voltage is the fastest way to get the energy level up.

Two of the devices tested are shown in Figures 24 and 25 along with the scope traces from the shots. Figure 24 shows a 32x80-µm n-phos Si SCB which fired at 12-v while Figure 25 shows the 90x270-µm n-phos Si SCB which fired at 20-v. The 90x270u SCB took much longer time to fire (more deposited energy).

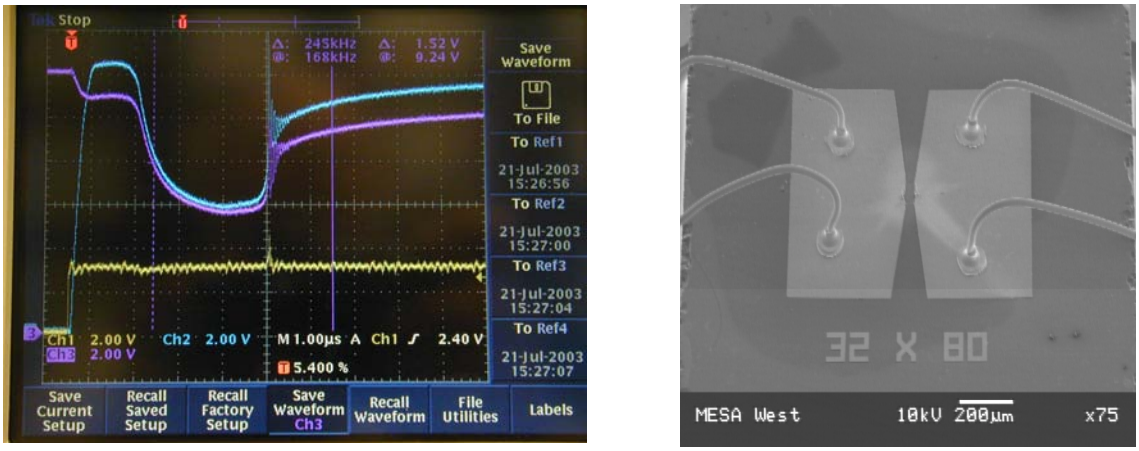

Figure 24. 32x80u n-phos Si SCB fired at 12v.

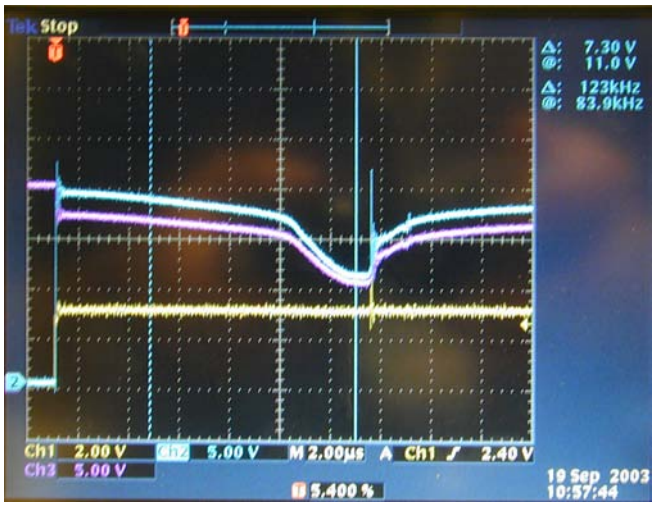

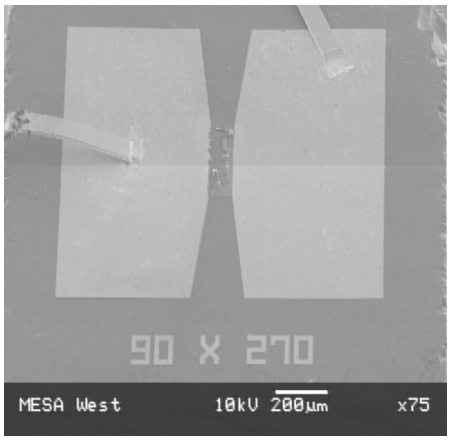

Figure 25. 90x270u n-phos Si SCB fired at 20v.

This page intentionally left blank.

Size And Shape Evaluation

An attempt was been made to determine the source characteristics that would be needed to monitor a microexplosive from a nearby borehole in a reservoir by using data from previous testing results and some analysis of the expected output. These studies provide an estimate of source strength required and optimal frequency (rise time).

The equations given here are derivations given by Aldridge[6] of an explosive point source in a uniform material. The acceleration in the far field, neglecting attenuation, is derived as

$$\vec{a}(R,t) = \frac{3E_o}{16\pi\rho V_p V_s^2 R} w'''\left(t - R/V_p\right)\vec{e}_a \ ,$$

where R is the distance from the source, t is the time, E_o is the energy imparted, ρ is the rock density, V_p is the compressional wave velocity of the rock, V_s is the shear wave velocity of the rock, w''' is the third derivative of a normalized waveform that models the source, and $\vec{e}_a$ is the acceleration direction unit vector. Taking the simplest case of a sinusoidal waveform,

$$w = \sin(2\pi f t) \ ,$$

the acceleration is

$$\vec{a}\left(R,t\big|_{\max}\right) = \frac{3E_o\pi^2 f^3}{2\rho V_p V_s^2 R}\vec{e}_a \ ,$$

where $t\big|_{\max}$ is the time at which the acceleration is a maximum and f is the frequency of the wave form.

Using typical values for sandstone rocks that are hydraulically fractured (ρ=2400 kg/m^3, V_p=4500 m/sec, V_s=3000 m/sec) and a 1 joule source strength, this results in an acceleration

$$\left|\vec{a}\left(R,t\big|_{\max}\right)\right| = 1.55x10^{-8}\,\frac{f^3}{R} \quad (\mu g's) \, .$$

Table 2 shows some relationships between distance and frequency for a 1 joule source.

Table 2. Acceleration (μg) at monitoring station due to distance and frequency

R(m)	10 Hz	100 Hz	1000 Hz	2000 Hz
10	.00000155	.00155	1.554	12.43
20	.0000008	.00077	0.777	6.22
50	.0000003	.00031	0.311	2.49
100	.00000016	.000155	0.155	1.24
200	.00000008	.000077	0.078	0.62
500	.00000003	.000031	0.031	0.25

Given that a minimum detectible acceleration is on the order of 10 μg, it is clear that there is little chance of measuring anything at low frequencies. However, for frequencies greater than 1000 Hz, and particularly at a typical maximum measurement frequency of 2000 Hz, it is only necessary to have imparted energies of a few tens of joules to have sufficient strength. However, it is never clear how much of the available energy is actually imparted to the rock as seismic energy (probably on the order of 10%). Thus, explosives having a few hundred joules to as much as a few thousand joules of energy are probably needed in order to monitor it at distances of 100 m. If the formation is seismically noisy, then it will require even higher levels.

This analysis also suggests that the rise time of the explosive or other energetic material be fast enough to generate large amounts of energy in the 2000 Hz frequency range. This would suggest that a rise time something on the order of 0.1 msec is required as a minimum.

As a check on this calculation, there are old some data where 3.5 gm perforation shots were monitored using accelerometers at a distance of 210 ft (64 m). For these shots, the background noise was 1 μg rms and the signal strength was 70 dB above the noise. Converting to peak values and multiplying by 70 dB (3,162), there was a signal strength of about 4,400 μg. Although the composition of the explosive material was not recorded, it is assumed that is was RDX powder. The energy content of the explosive, using an estimate of 4,000 joules/gm, has a total of about 14,000 joules. Since most of the recorded energy was near 2,000 Hz, the response equation suggests that a 4,400 μg response at 64 m would have probably required about 2,200 joules of coupled energy. Given an input of 14,000 joules, this test suggests that the coupling was 16% efficient, which is actually quite high. This may be because the actual material was more energetic, the shape charge provides a more focused energy source, or any number of other possible explanations. Nevertheless, the experimental data and the model both seem to offer a reasonable amount of agreement.

It appears that quantities of energetic material ranging from 0.1 to 1.0 gm may be sufficient for the purposes of the project. Assuming a density of 1.7 gm/cc as a probably high value, the microexplosive particle will require 0.2 – 2.0 cm^3 of volume without the covering and/or triggering. A spherical particle would need to have a diameter of 0.4 – 0.8 cm to enclose this volume.

While this size is appropriate for FracPacks[5] (hydraulic fractures that are performed in very low modulus rocks and result in fracture widths of several centimeters) and some other fracture operations, the large size does limit the application considerably. Another approach is to design an appropriate shaped particle (e.g., torpedo) that will reduce the cross-section by increasing the length. Such an approach would not work for Newtonian fluids, where such particles would tend to turn broadside to the flow direction and likely bridge. However, the non-Newtonian cross-linked gels have characteristics that cause the long axis of an elongated particle to align with the flow direction. In such a case, a cylinder that was thrice as long as the diameter would require diameters of 0.3 – 0.6 cm to enclose the volume, providing some additional capability.

To evaluate the likelihood of flow alignment of elongated particles, the work of Joseph, Huang and colleagues[7-10] has shown that bodies behave differently in non-Newtonian fluids than they do in Newtonian fluids. Elasticity of the fluid turns the long axis of the bodies along the stream direction when a critical elasticity number is exceeded. The cross-linked gel fracturing fluid in use today are such that the elasticity number is well above that needed for aligned flow. These types of fluids are used in about 50% of all fracture operations today, which makes a torpedo design practical in these cases.

The likelihood of a particle aligning in the flow stream depends upon the aspect ratio (major axis/ minor axis) of the particle, *a/b*, and the Reynolds and Deborah numbers, given by

$$\mathrm{Re} = \frac{\rho_f U a}{\mu}$$

and

$$\mathrm{De} = \frac{U\lambda}{a} \ ,$$

where U is the velocity, ρ_f is the fluid density, μ is the viscosity, and $\lambda$is the relaxation time of the fluid. However, it is more useful to recast these into elasticity and Mach numbers by

$$\mathrm{E} = \mathrm{De}/\mathrm{Re}$$

and

$$\mathrm{M} = \sqrt{\mathrm{Re}\,\mathrm{De}} \ .$$

The elasticity number is the ratio of elastic and inertia forces in the fluid while the Mach number (for these viscoelastic fluids) is the ratio of the velocity to the shear-wave speed, where the shear wave speed is given by

$$V_s = \sqrt{\frac{\mu}{\lambda\rho_f}} \ ,$$

which is quite slow for these types of fluids.

The critical elasticity number appears to be about 3, which marks the border between effective Newtonian and effective viscoelastic behavior. The critical Mach number is around unity, so that the velocity is greater than the shear-wave velocity of the fluid.

Unfortunately, relaxation times are not compiled for these cross-linked gels, as the only pertinent parameters for hydraulic fracturing are the consistency index, *n'*, the absolute consitency, *k'*, and the yield stress, τ_y. Nevertheless, laboratory experiments have shown that these fluids exhibit the elastic behavior specified above. Typically, proppant particles are found to "chain" as they progress along the flow stream. This "chaining" only occurs under the same conditions as does long-axis alignment (it can be shown that the same forces create this behavior as those that align the object), so it is clear that the fluid behavior is appropriate.

Assuming a typical fracture injection rate of 50 bpm into a 2 cm wide crack that is 30 m in height, the velocity through the crack would be about 0.09 m/sec. Viscosities of these fracturing fluids are usually several thousand centipoises, so a value of about 2,000 would be average. For a torpedo with a diameter of 0.3 cm, the Reynolds number would be about 0.13 (essentially creep flow). For an elasticity ratio greater than 3, the Deborah number would need to be three times this value, or 0.4. In such a case, the relaxation time would need to be 0.014 sec or longer. However, to satisfy the Mach number constraint, the Deborah number would need to be greater than 7.7, requiring a relaxation time of 0.27 sec. The fracturing fluids appear to have relaxation times on the order of seconds, based on observation of some of

their physical characteristics. For example, if some fracturing fluid is partially poured from one beaker into another and then stopped, the poured material will slowly return to the original beaker with the process taking from seconds to tens of seconds depending on the fluid.

Unfortunately, the relaxation times for these fluids are generally unknown at this time and some characterization would be worthwhile before widespread use of this phenomenon should occur. The one study that was found on this problem (Prud'homme[11]) gave relaxation times of 5.7 and 7.7 sec for two typical gels. More data are obviously needed; however, acquiring and testing these proprietary materials is outside of the scope of this effort.

Seismic Response In A Fracture

While detailed seismic modeling of this process requires the pressure pulse characteristics of the source within a fluid/proppant filled fracture to assess coupling, attenuation, frequency characteristics and other parameters, some calculations of performance can be made with available wave-code calculations. These initial calculations have suggested that approximately 100 milligrams of explosive material could be observed at 100 m distance, but some additional work needs to be done on assessing the coupling of the detonation to the fracture wall.

Seismic modeling has been performed to characterize the amount of energy coupled into the rock from the fluid-filled fracture and the type of waveforms generated (e.g., are they analyzable). Results have shown that a significant amount of energy is coupled directly into the rock and that the amount of energy and the shape of the waveforms are somewhat dependent on the crack width and source pulse shape. Modeling was performed with an in-house seismic code named ELASTI.[12] Essentially, a water-filled crack embedded in a sandstone matrix was gridded and a seismic source having a Ricker wavelet pulse was initiated at time zero. The resulting waveforms and amplitudes were then analyzed and processed.

Table 3 gives a listing of the various cases that were run. These include various grid sized, various crack sizes, and several frequencies. Although the crack sizes are considerably larger than those encountered in typical fracturing applications, the coupling through the fluid into the rock was of primary interest and it is believed that coupling behavior will be similar for smaller crack widths.

Figure 26 shows one of these calculations at 7 msec after the energy release, while Figures 27-30 show results at 11, 13, 17 and 21 msec, respectively. The energy is well-focused outward, except for end effects with the fracture as the pressure wave moves up and down. The scale is relative to the size of the initial pressure wave (amplitude of 1) and needs to be rescaled to velocity through the acoustic impedance of the fluid and other factors. The maximum amplitude in Figure 26 is about $9x10^{-6}$ at about 30 m from the fracture. When rescaled and adjusted for 1/R decay, the result suggests that about 30-40% of the pressure wave within the fracture is coupled into the rock. This case is a fairly wide fracture (for ease of numerical solution), but narrower fractures would intuitively couple more energy into the rock.

Waveforms along both horizontal lines and across vertical sections for a horizontal velocity sensor (e.g., geophone) are shown in Figures 31 and 32. Only the compressional wave is observable in this case.

Finally, the amplitude decay of the velocity as the wavefronts cross the crack-rock interface are shown in Figures 33-35 for crack widths of 0.25, 0.5 and 0.75 m, respectively and for a grid size specified by the spacing for each test. While there appears to be some interaction of the wavefront amplitude with the crack (and this may be primarily numeric artifacts), the amplitude decay is very similar to the 1/R decay that would typically be observed in a material and there does not appear to be any large losses at the interface.

Table 3. Summary of model runs for seismic calculations

	Crack Width	Frequency	Grid Spacing (m)	Time Step
Model 18	1.0	2000	0.01 x 0.05 x 0.01	4.0e-7
Model 19	0.75	2000	0.01 x 0.05 x 0.01	4.0e-7
Model 20	0.50	2000	0.01 x 0.05 x 0.01	4.0e-7
Model 21	0.25	2000	0.01 x 0.05 x 0.01	4.0e-7
Model 22	2.00	2000	0.01 x 0.05 x 0.01	4.0e-7
Model 23	1.00	4000	0.01 x 0.05 x 0.01	4.0e-7
Model 24	0.75	4000	0.01 x 0.05 x 0.01	4.0e-7
Model 25	0.50	4000	0.01 x 0.05 x 0.01	4.0e-7
Model 26	0.25	4000	0.01 x 0.05 x 0.01	4.0e-7
Model 27	2.00	4000	0.01 x 0.05 x 0.01	4.0e-7
Model 28	1.00	500	0.01 x 0.05 x 0.01	4.0e-7
Model 29	0.75	500	0.01 x 0.05 x 0.01	4.0e-7
Model 30	0.50	500	0.01 x 0.05 x 0.01	4.0e-7
Model 31	0.25	500	0.01 x 0.05 x 0.01	4.0e-7
Model 32	2.00	500	0.01 x 0.05 x 0.01	4.0e-7
Model 33	1.00	500	0.05 x 0.05 x 0.05	1.0e-6
Model 34	0.75	500	0.05 x 0.05 x 0.05	1.0e-6
Model 35	0.50	500	0.05 x 0.05 x 0.05	1.0e-6
Model 36	0.25	500	0.05 x 0.05 x 0.05	1.0e-6
Model 37	2.00	500	0.05 x 0.05 x 0.05	1.0e-6
Model 38	1.00	2000	0.05 x 0.05 x 0.05	1.0e-6
Model 39	0.75	2000	0.05 x 0.05 x 0.05	1.0e-6
Model 40	0.50	2000	0.05 x 0.05 x 0.05	1.0e-6
Model 41	0.25	2000	0.05 x 0.05 x 0.05	1.0e-6
Model 42	2.00	2000	0.05 x 0.05 x 0.05	1.0e-6
Model 43	1.00	4000	0.05 x 0.05 x 0.05	1.0e-6
Model 44	0.75	4000	0.05 x 0.05 x 0.05	1.0e-6
Model 45	0.50	4000	0.05 x 0.05 x 0.05	1.0e-6
Model 46	0.25	4000	0.05 x 0.05 x 0.05	1.0e-6
Model 47	2.00	4000	0.05 x 0.05 x 0.05	1.0e-6

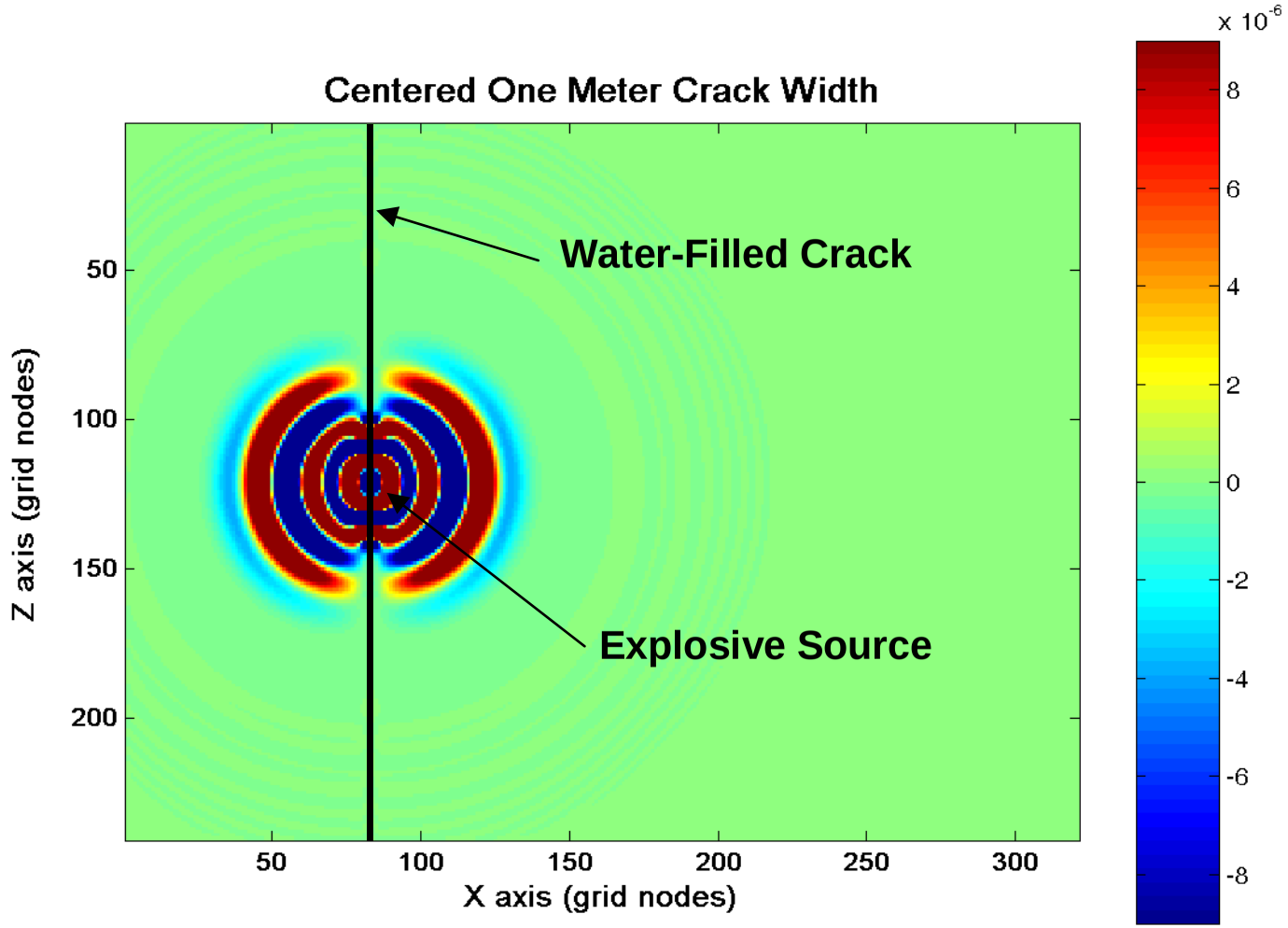

Figure 26. Calculation of explosive behavior at 7 msec.

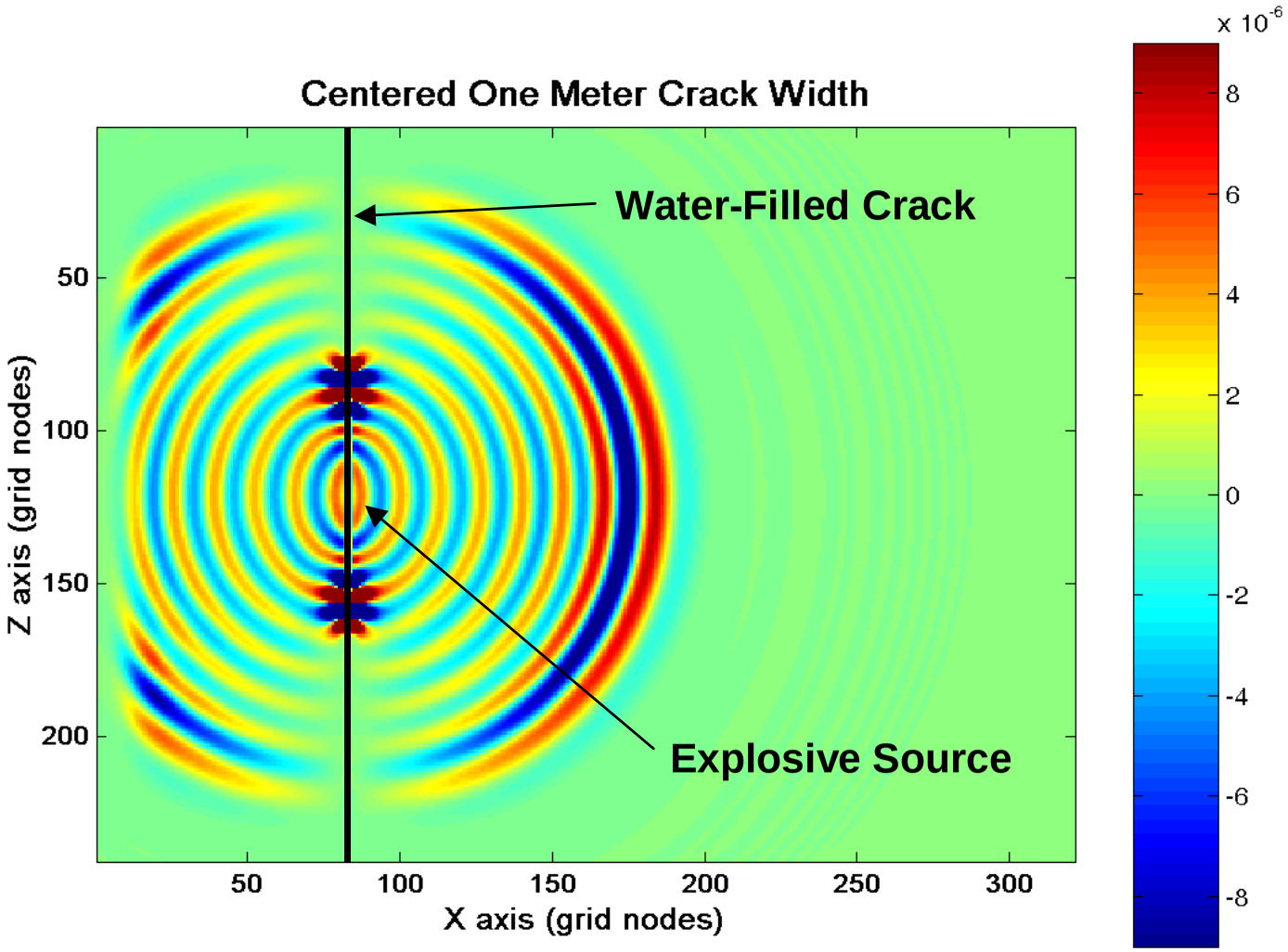

Figure 27. Calculation of explosive behavior at 11 msec.

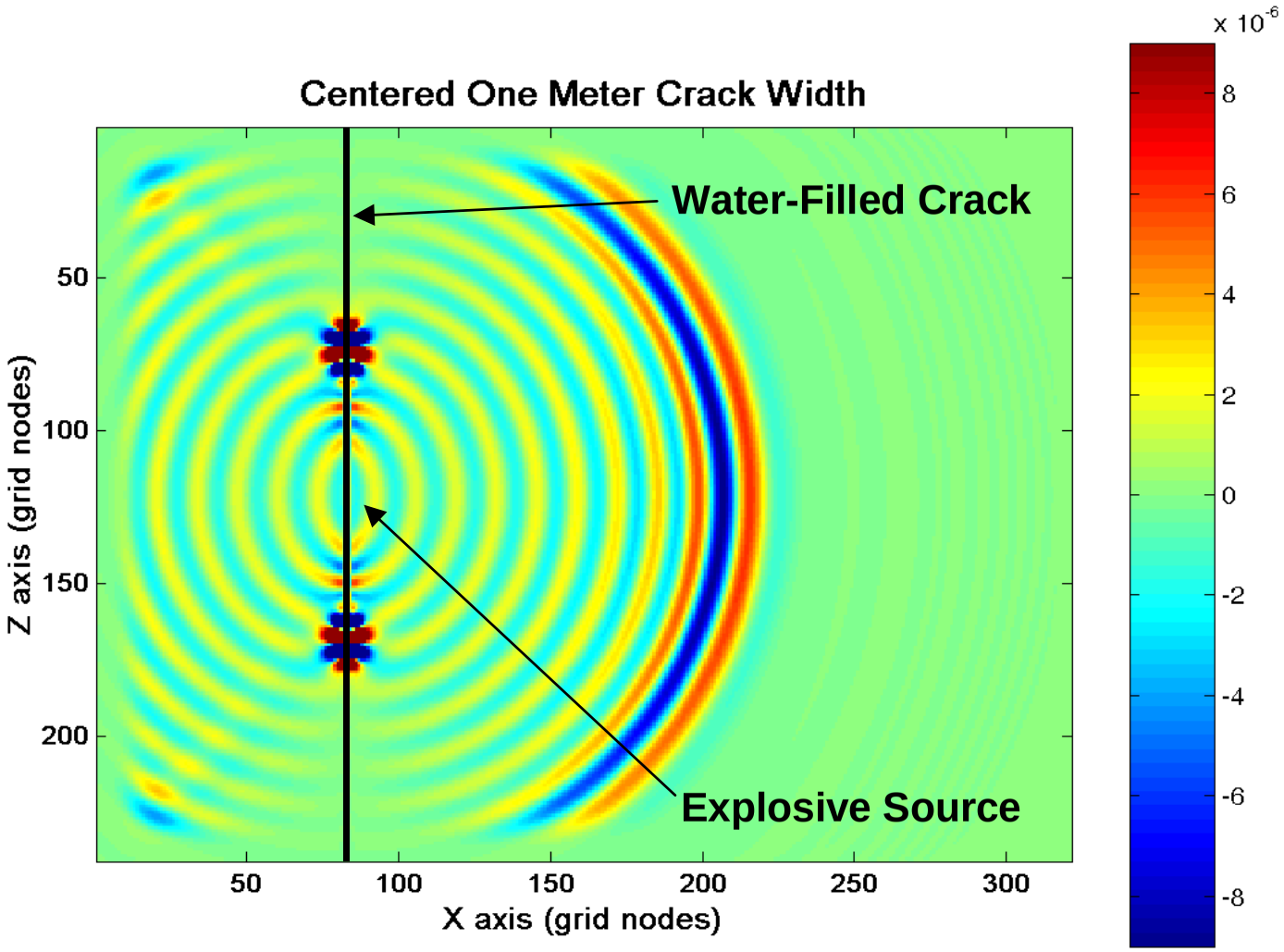

Figure 28. Calculation of explosive behavior at 13 msec.

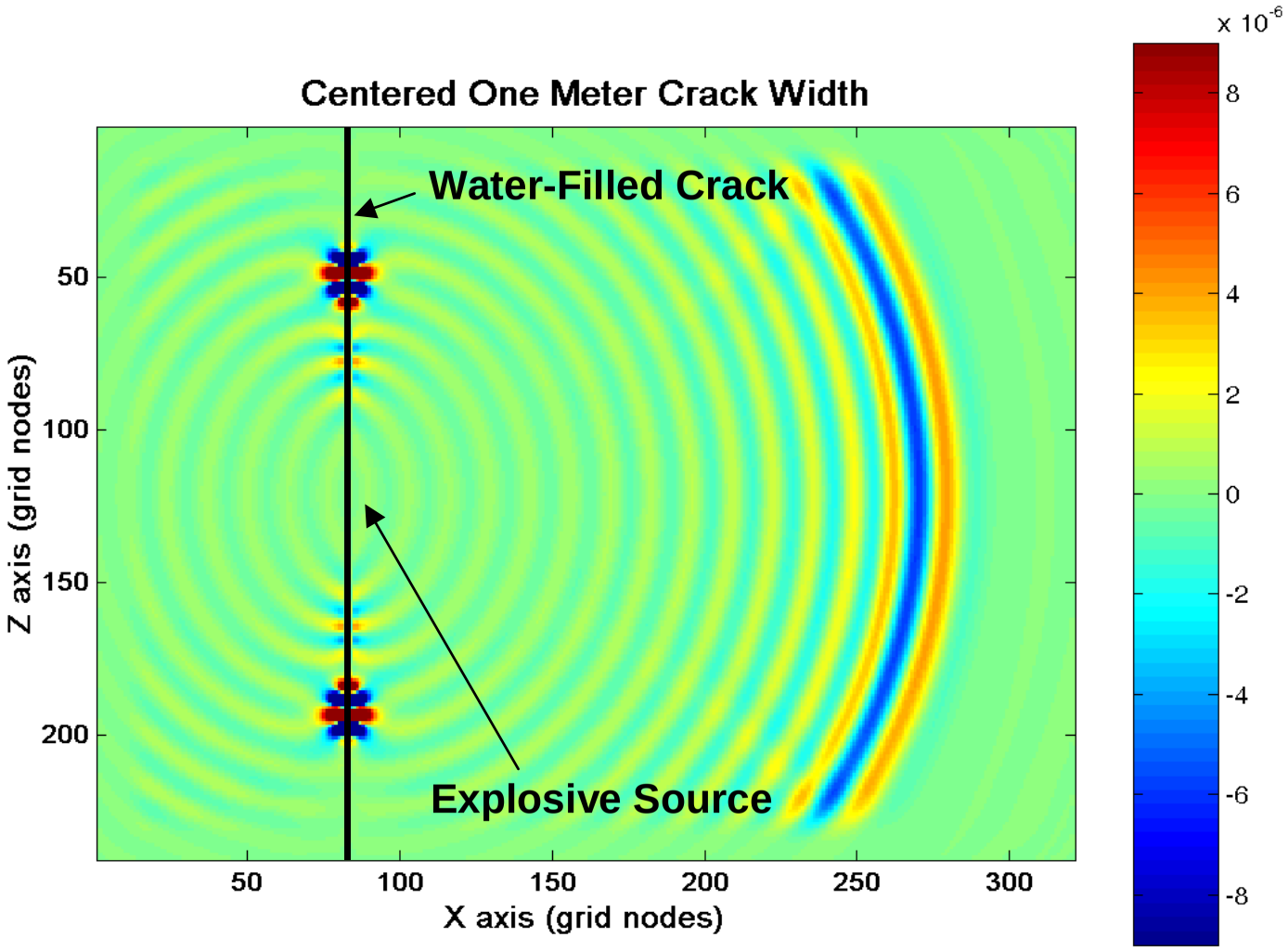

Figure 29. Calculation of explosive behavior at 17 msec.

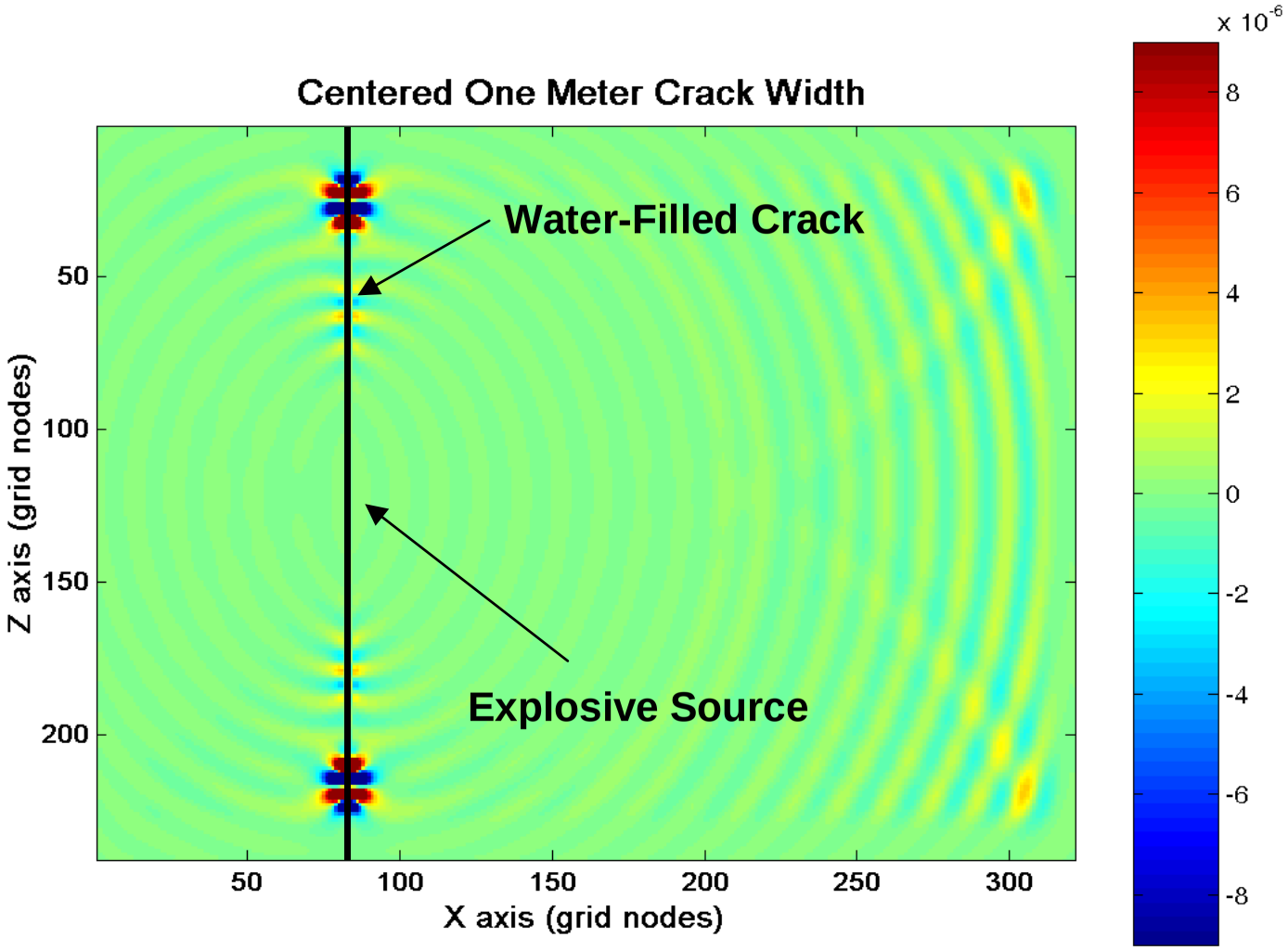

Figure 30.

Calculation of explosive behavior at 21 msec.

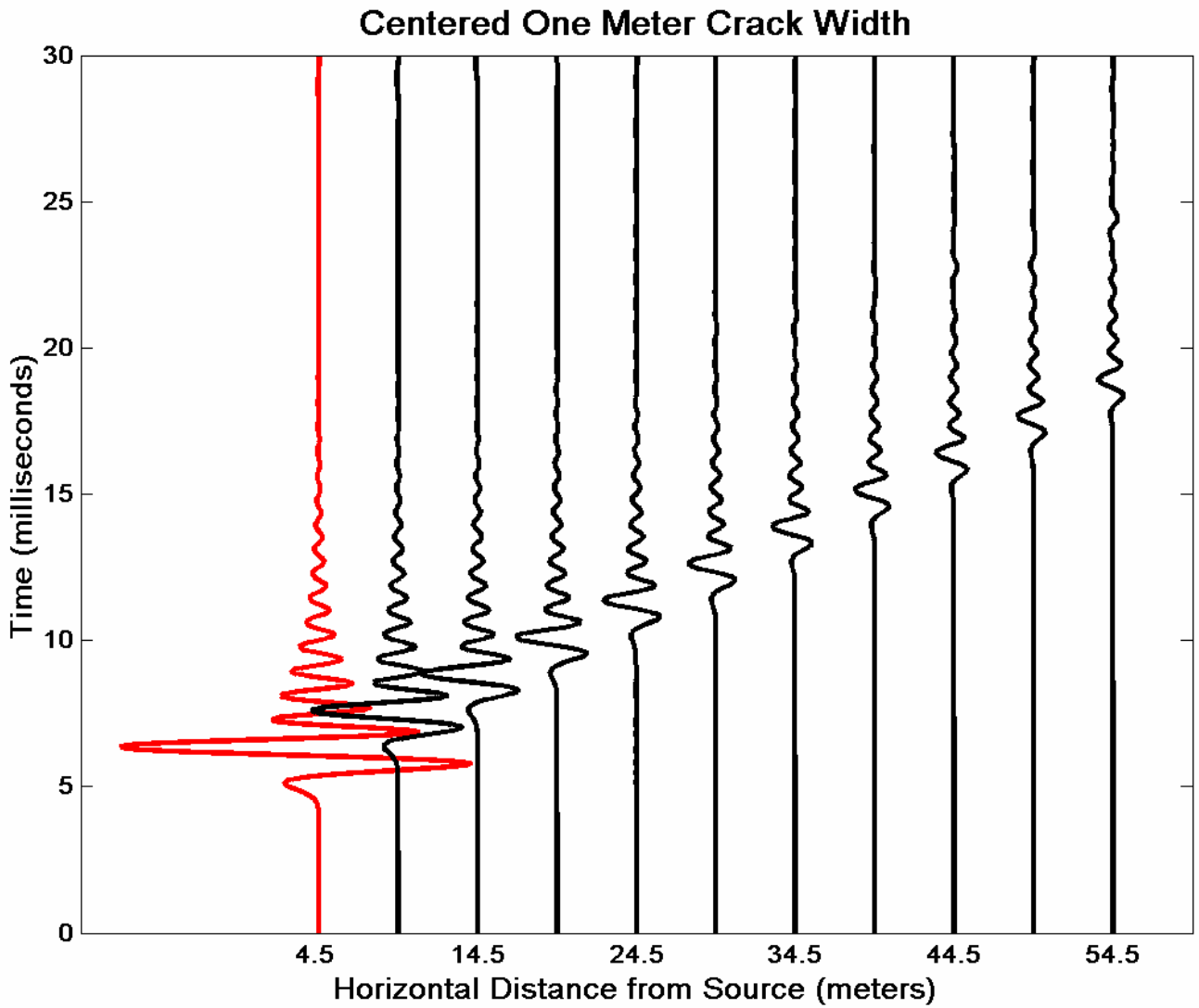

Figure 31. Waveforms along centerline at various distances from source.

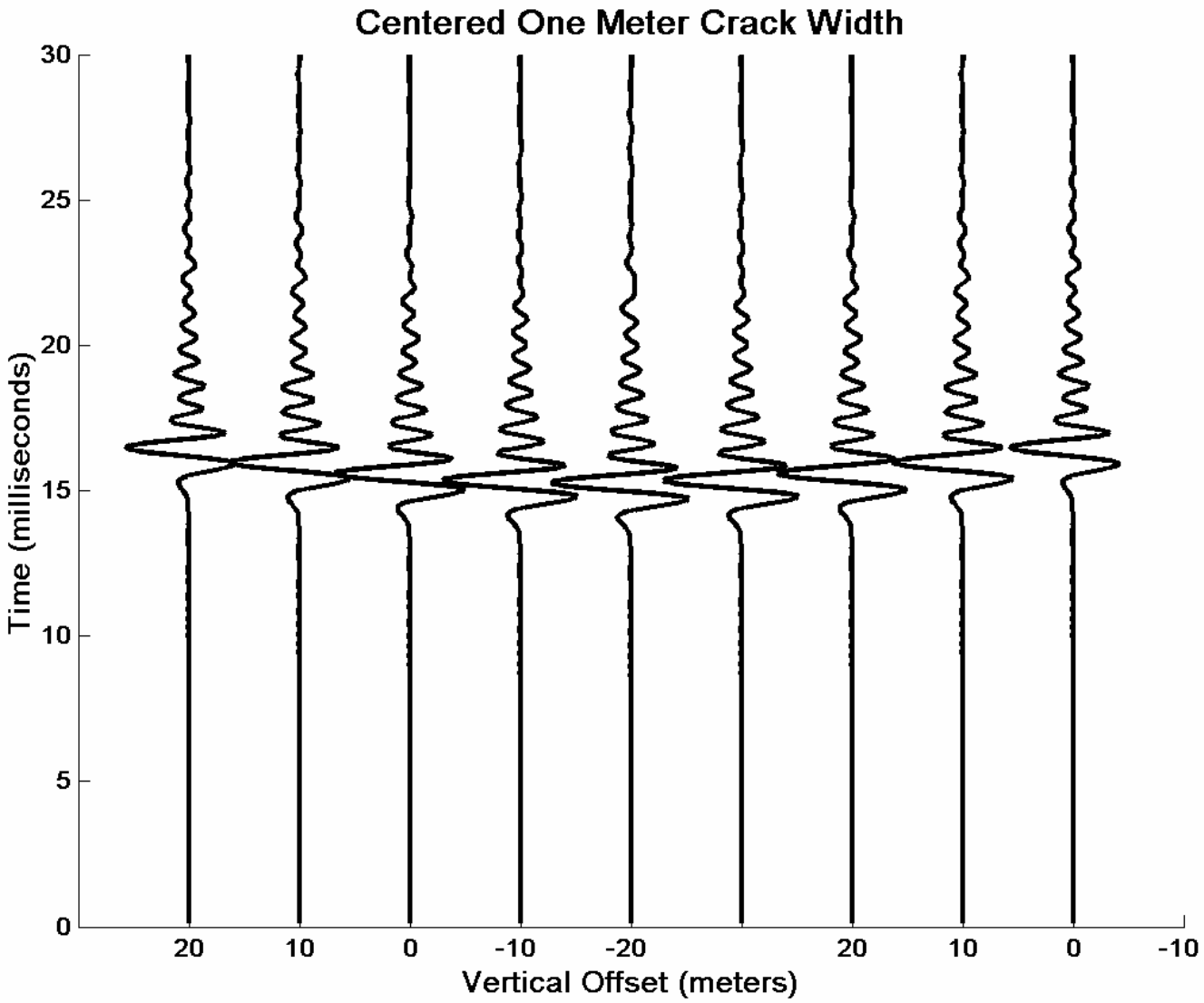

Figure 32. Waveforms for a vertical cross-section at approximately 40 m from source.

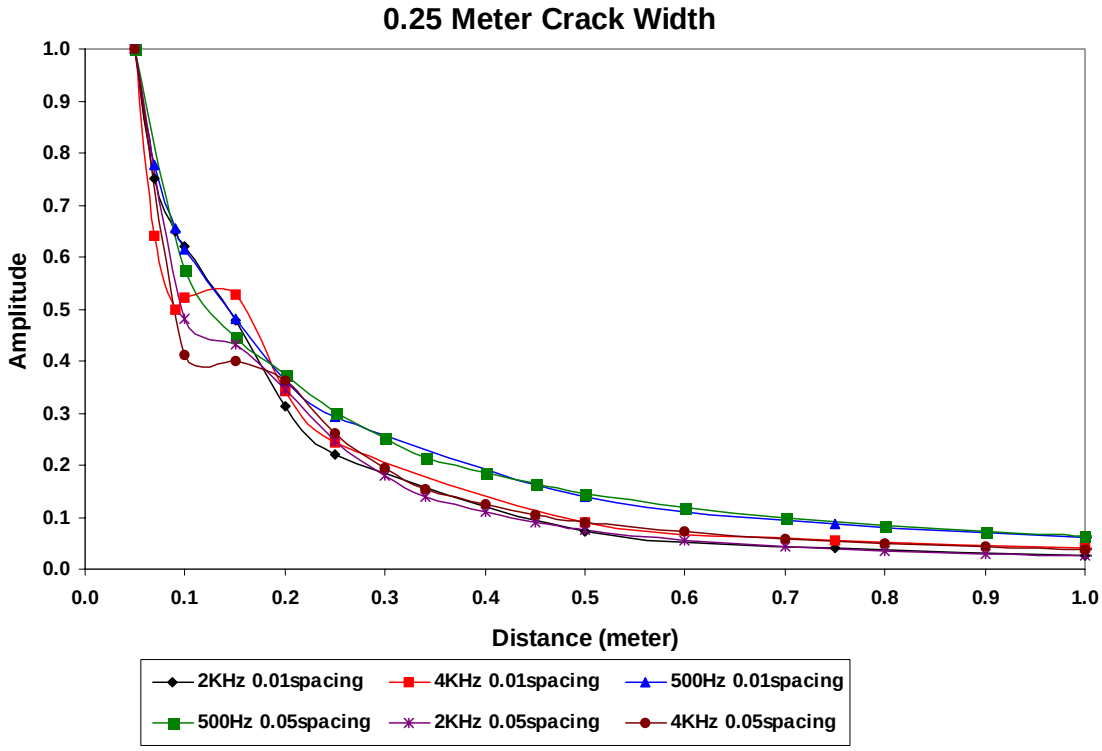

Figure 33. Normalized velocity amplitudes as a function of distance from source, 0.25 m crack.

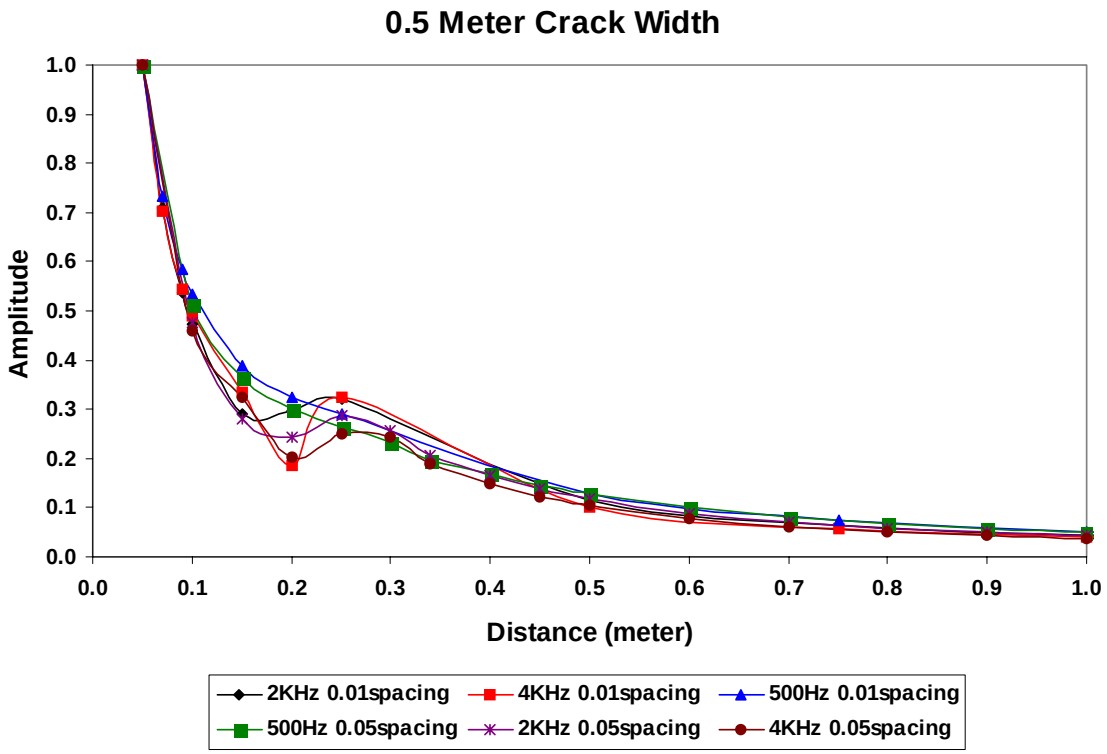

Figure 34. Normalized velocity amplitudes as a function of distance from source, 0.5 m crack.

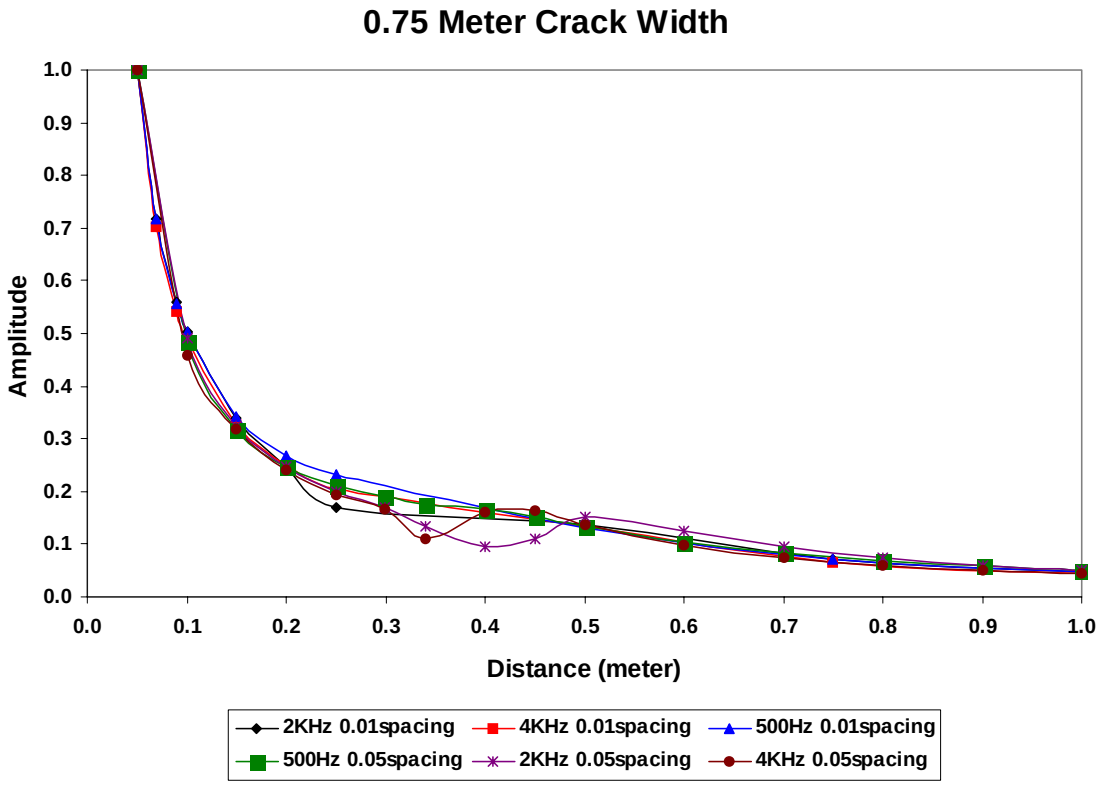

Figure 35. Normalized velocity amplitudes as a function of distance from source, 0.75 m crack.

This page intentionally left blank.

Chamber Tests

The objective of this test series was to detonate several types of explosive materials and measure the pressure pulse response in a water-filled cavity. The sample explosive material was placed inside a containment vessel, the vessel was filled with water, and pressure transducers were used to record shock impulse data such as pulse amplitude, pulse duration, and pulse time of arrival.

Overview

All experiments and testing were conducted at Sandia National Laboratories (Building 9930). A containment vessel was utilized for water retention and fragment suppression. The containment vessel was setup inside the Explosive Component Room and the pressure transducers were connected to a Lecroy oscilloscope. Pressure impulse data such as pulse amplitude, pulse width, and time of arrival were recorded and retrieved via electronic media. A TC501 Fireset was utilized to ignite the detonators.

Containment Vessel

The containment vessel (rated for 1.25g of PETN) was used as a water tank and for fragment suppression (Figure 36). The explosive pellets (encapsulated inside a blasting cap) were placed inside the containment vessel, the vessel was filled with water, the explosive pellet was detonated and pressure impulse data was recorded for each shot.

Figure 36. Containment Vessel

Explosive Characterization and Description

The explosive powder was pressed into a pellet to specific density and packed into a blasting cap. A Pyropak BGZD head electric match was used as the initiating device (Figure 37).

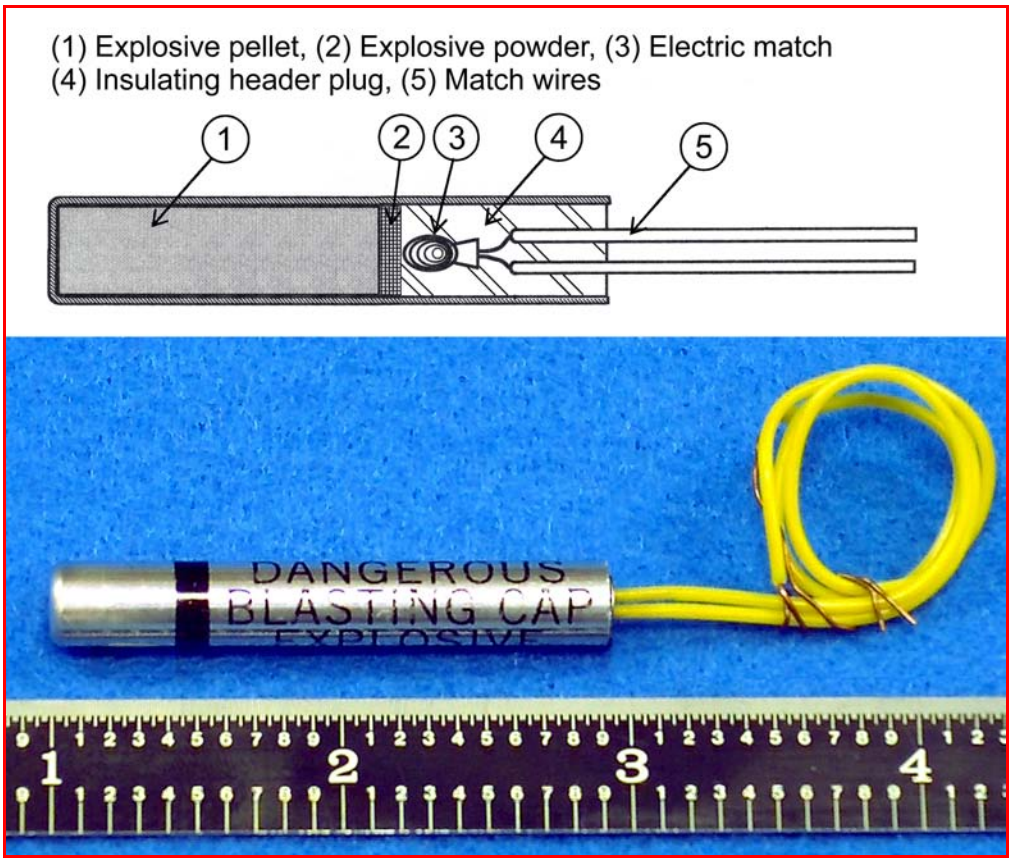

Figure 37. Explosive capsule description.

Several types of explosive materials were pressed and encapsulated into these blasting caps. The explosive materials used in this test series are as follows:

PETN (Pentaerythritoltetranitrate)
The PETN was Type I material. It was originally prepared for use in EBW detonators and has a mean surface area of 4000 cm_2/g as determined by the Fisher sub-sieve method. The PETN pellets were pressed to a density of 1.63 g/cc.

RDX (Cyclotrimethylenetrinitramine)
The RDX was Grade II, Class B material. The particle size distribution of this RDX was not measured, however Grade II, Class B material has a screening requirement where 75% of the material must pass through a number 325 sieve (44 μm). The RDX pellets were pressed to a density of 1.6 g/cc.

BNCP (Tetraammine-cis-bis-(5nitro-2H-tetrazolato-N^2)cobalt(III) perchlorate)
The BNCP was Class 4 material. The particle size of the BNCP was very fine particle distribution and sieved to less than 40 microns. The BNCP pellets were pressed to a density of 1.597 g/cc.

DDNP (Diazodinitrophenol)
The DDCP was Class 4 material. The particle size of the DDNP was very fine particle distribution and sieved to less than 40 microns. The DDNP pellets were pressed to a density of 1.63 g/cc.

THKP (Titanium Subhydride (0.65) Potassium Perchlorate)
The THKP was Class 4 material and the THKP pellets were pressed to a density of 1.8 g/cc.

$MgAgNO_3$ (Magnesium Silver Nitrate)
The $MgAgNO_3$ is classified as a pyrotechnic. The mixture consisted of 30% Mg and 70% $AgNO_3$. The $MgAgNO_3$ pellets were pressed to a density of 1.83 g/cc.

Test Procedure

A vessel certification shot was necessary to rate the containment vessel at 1.0 g. of explosive. A 1.25 g. of PETN was first detonated inside the containment vessel to certify the vessel. All other subsequent shots were conducted to obtain actual pressure impulse data. Table 4 describes all shots conducted in this test series and the purpose of each shot. Test #1 was conducted to certify the containment vessel at 1.0 g. of explosives. Test #2-3 were conducted to calibrate the pressure transducers to a reference level. Tests #4-18 were conducted to obtain pulse amplitude, pulse width, and pulse time of arrival.

Table 4. Test procedure and experiment setup

Test #	Date	Explosive Type	Explosive Quantity	Purpose
#1	4/29/03	PETN	1.25 g.	Vessel Certification
#2	6/3/03	RDX	1.111 g.	Transducer Calibration
#3	6/3/03	RDX	1.111 g.	Transducer Calibration
#4	6/3/03	RDX	1.111 g.	Transducer Calibration
#5	7/2/03	BNCP	1.008 g.	Pressure Impulse Data
#6	7/2/03	BNCP	1.009 g.	Pressure Impulse Data
#7	7/2/03	BNCP	1.009 g.	Pressure Impulse Data
#8	7/2/03	DDNP	1.008 g.	Pressure Impulse Data
#9	7/2/03	DDNP	1.008 g.	Pressure Impulse Data
#10	7/2/03	DDNP	1.008 g.	Pressure Impulse Data
#11	7/25/03	THKP	1.008 g.	Pressure Impulse Data
#12	7/25/03	THKP	1.009 g.	Pressure Impulse Data
#13	7/25/03	$MgAgNO_3$	1.008 g.	Pressure Impulse Data
#14	7/25/03	$MgAgNO_3$	1.009 g.	Pressure Impulse Data
#15	7/25/03	$MgAgNO_3$	1.008 g.	Pressure Impulse Data
#16	7/26/03	$MgAgNO_3$	1.008 g.	Pressure Impulse Data
#17	7/26/03	$MgAgNO_3$	1.008 g.	Pressure Impulse Data
#18	7/26/03	$MgAgNO_3$	1.007 g.	Pressure Impulse Data

Data Analysis

The explosive pellets were detonated inside a 10-inch diameter, 10-inch long cylindrical containment vessel. The initial radial impulse shock propagated through the water and reached the bottom of the vessel (pressure transducer) before any other rarefactions could interfere with the initial measurement. Subsequently, lateral rarefactions from the side-walls propagated to the transducer and produce a second impulse. A third pulse was generated by the top plate rarefactions and many other smaller rarefactions were subsequently generated as illustrated in Figure 38.

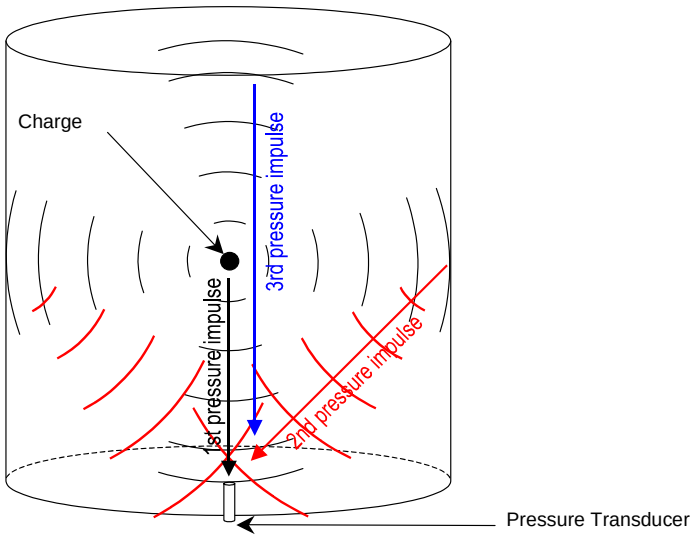

Figure 38. Containment vessel shock wave propagation.

For underwater shock wave below 29,000 psi, the wave velocity closely approaches the standard acoustic velocity of ~1500m/s or 12μs/in. In our experimental arrangement, the pressure transducers were 5 inches away from the charge, therefore it would take 60μs for the 1st initial impulse to reach the transducer. The detonation time of the pellet/blasting cap was calculated to be approximately 10μs, therefore the time of arrival for the 1st shock impulse is calculated to be:

time of arrival; $t_1 \approx t_{5\text{-inches}} + t_{detonation} = 60\ \mu s + 10\ \mu s = 70\ \mu s$

Therefore it will take approximately 70μs for the 1st impulse to reach the transducer as shown in Figure 39. The second rarefaction shock wave is approximated as follows:

time of arrival; $t_2 \approx t_1 + t_{7\text{-inches}} = 70\ \mu s + 84\ \mu s = 154\ \mu s$

Therefore it will take approximately 154μs for the 2nd rarefaction wave to reach the transducer as shown in Figure 39. The 3rd rarefaction shock wave is approximated as:

time of arrival; $t_3 \approx t_1 + t_{10\text{-inches}} = 70\ \mu s + 120\ \mu s = 190\ \mu s$

Therefore it will take approximately 190μs for the 3rd rarefaction wave to reach the transducer and so on. Many other cluttered rarefactions will subsequently follow the first three shock pulses, but their amplitude and duration may be too disorderly.

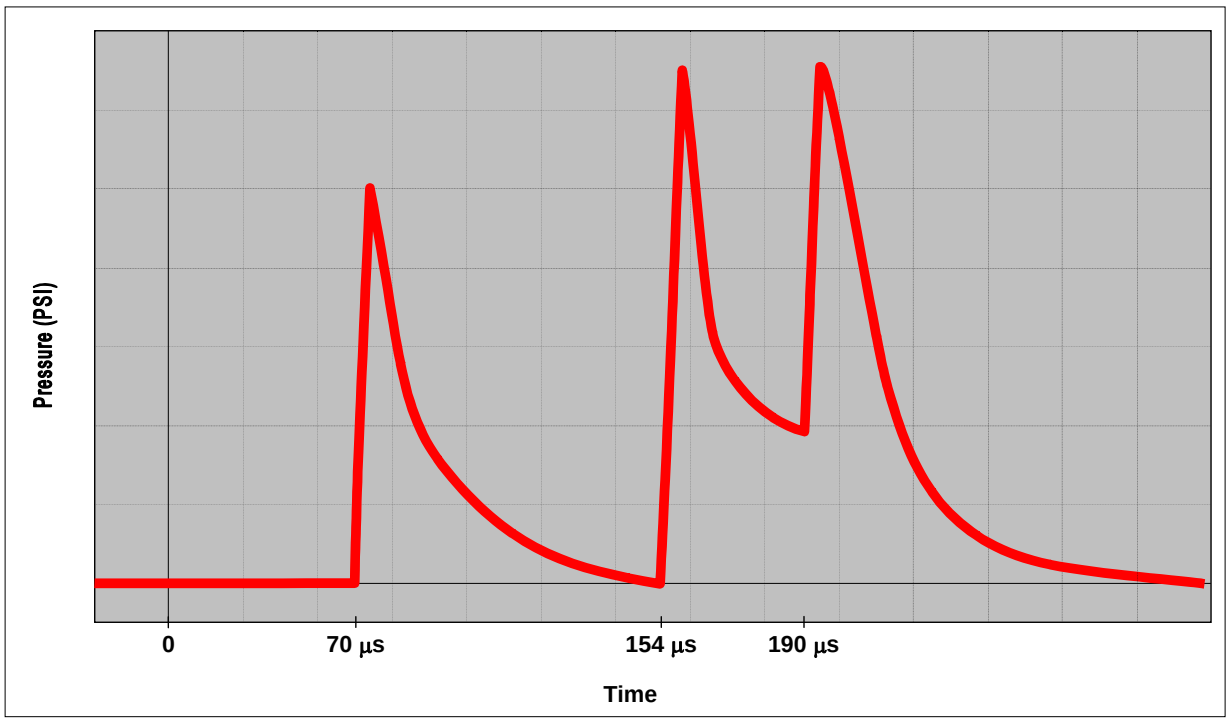

Figure 39. Calculated time-of-arrival of pressure pulse

Test Results

The following data plots are actual measurements from the pressure transducers. As predicted in our data analysis, the empirical test data follows the calculated shock wave calculations.

PETN

The 1st glitch in Figure 40 is due to the coupled fireset noise, which gives an indication of trigger and initial detonation. The 2nd impulse is the initial pressure pulse, the 3rd pulse is generated by the lateral side-wall rarefactions, and the 4th impulse is generated by the top-plate.

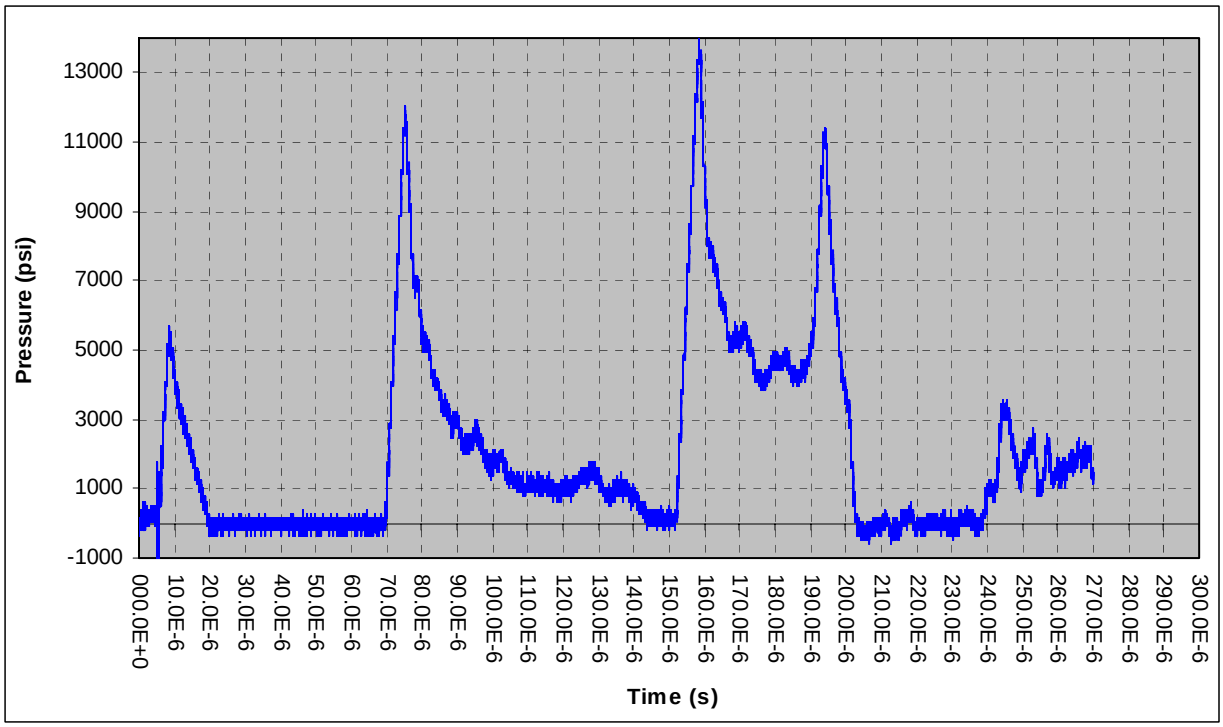

Figure 40. Characteristic PETN Pressure Pulse

RDX

The RDX pressure pulse in Figure 41 is very similar to that of PETN. Again, the 1st large impulse is due to the coupled fireset noise, and the 2nd, 3rd, and 4th pulses are the actual initial pressure pulse and the internal containment vessel wall rarefaction shock waves.

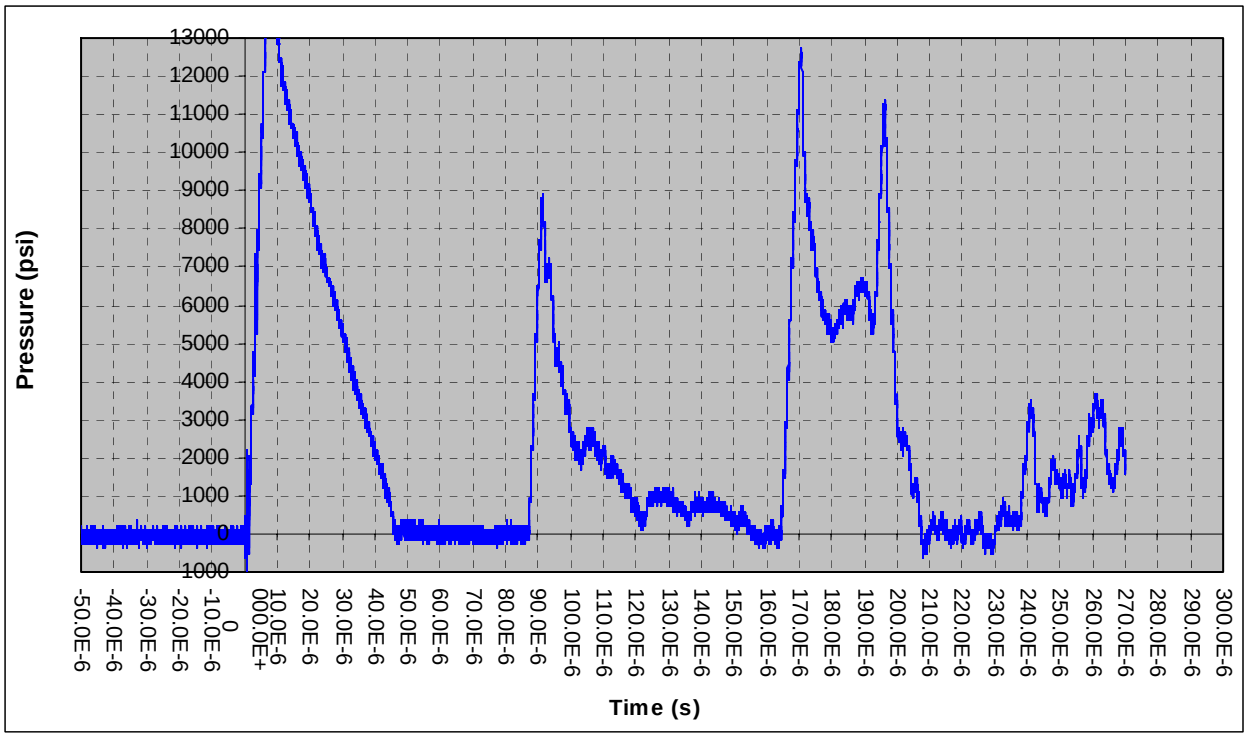

Figure 41. Characteristic RDX Pressure Pulse

BNCP

For this shot and all other subsequent shots, the coupled noise from the fireset was isolated from the transducer cables, therefore it no longer appears in the measured pressure pulse data.

The BNCP pressure pulse in Figure 42 is also similar to the PETN and RDX pressure pulses (with the exception of the coupled fireset noise). The 1st pulse is the initial pressure impulse followed by the shock wave rarefactions form the internal containment vessel walls.

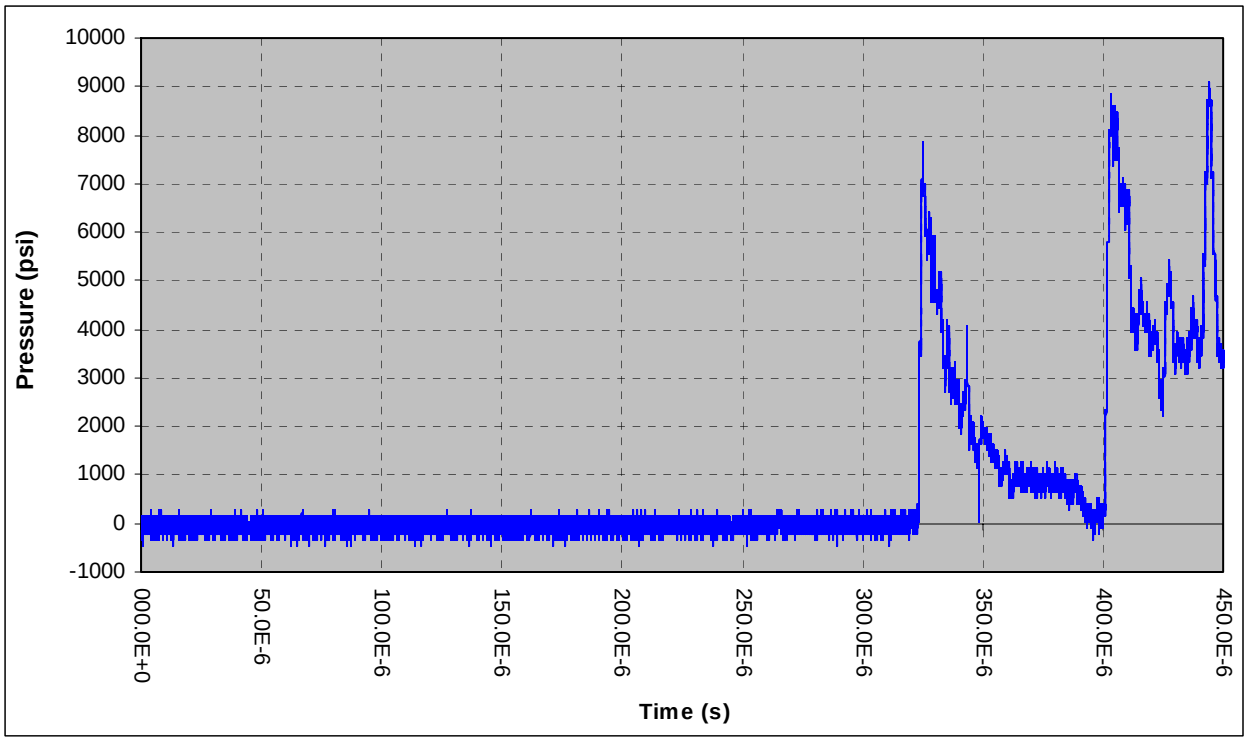

Figure 42. Characteristic BNCP Pressure Pulse

DDNP

The DDNP pressure pulse in Figure 43 shows a divergence from previous shots due to the DDNP explosive characteristics. DDNP is a less energetic material therefore having a much slower response. The initial shock impulse is not as sharp as the previous shots and the wall rarefaction waves begin to overtake the initial shock impulse.

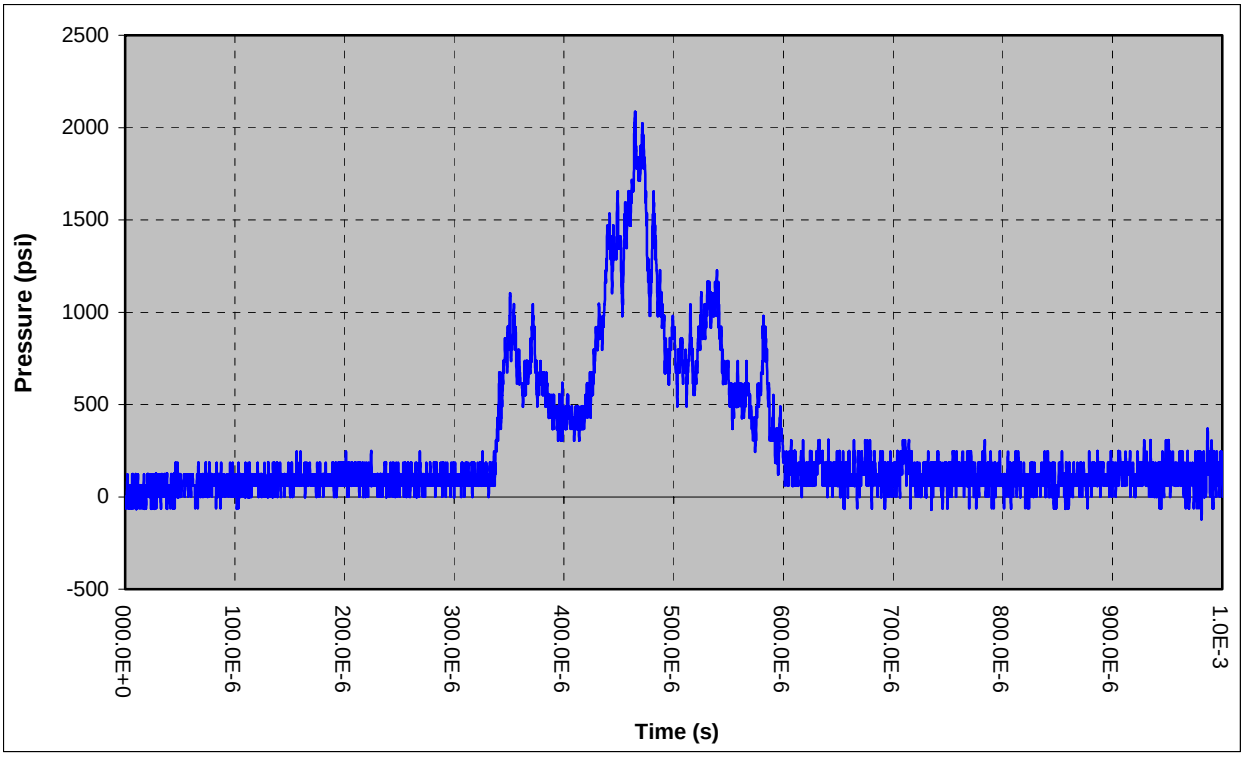

Figure 43. Characteristic DDNP Pressure Pulse

THKP

The THKP pressure pulse in Figure 44 is very similar to DDNP due to similarities in explosive characteristics. The initial shock impulse is less sharp and the wall rarefaction pulses overtake a great portion of the initial shock impulse.

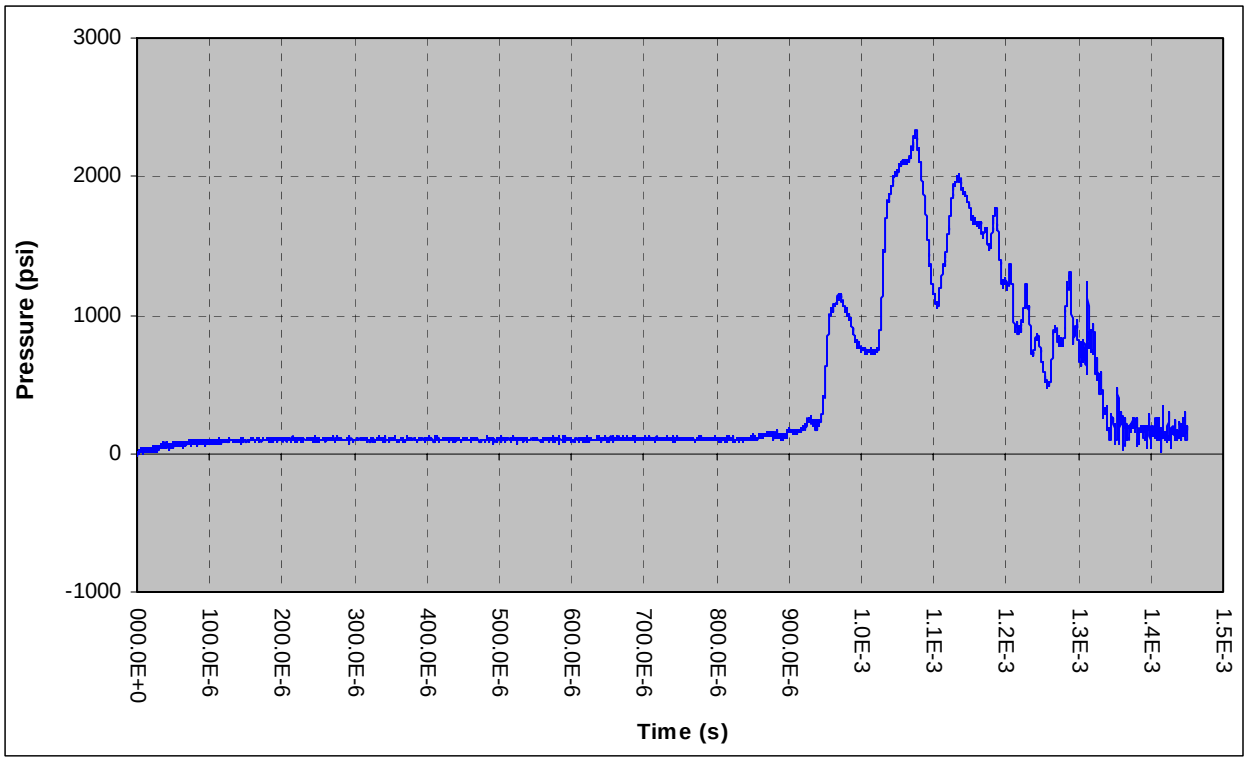

Figure 44. Characteristic THKP Pressure Pulse

$MgAgNO_3$

$MgAgNO_3$ a pyrotechnic, is the slowest and less energetic material of all materials tested. The $MgAgNO_3$ pressure pulse in Figure 45, although similar to DDNP and THKP, displays an initial shock impulse that is even less sharp and the wall rarefaction pulses completely overtake the initial shock impulse.

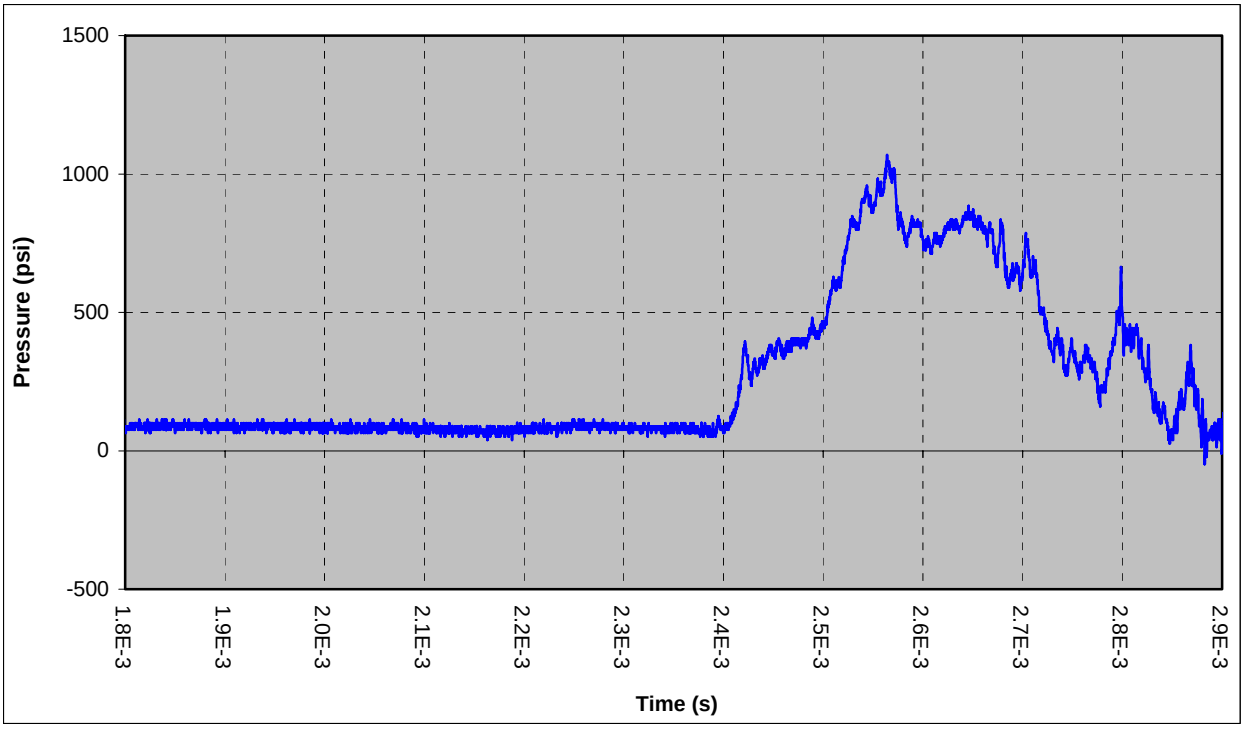

Figure 45. Characteristic MgAgNO3 Pressure Pulse

In summary, several types of explosive materials were tested to measure the pressure pulse response. The PETN, RDX, and BNCP appear to have an exceedingly fast response to be measure at the frequencies of interest (under 1000Hz). The DDNP, THKP, and $MgAgNO_3$ proved to be the preferred materials due to their slower response. Several efforts were initiated to test these preferred materials and measure other ideal material response characteristics.

This page intentionally left blank.

Concrete Block Test

The final stage of the microexplosive project was to conduct a field test in either a rock interface or concrete slab in order to evaluate the output of the microexplosive pellets in a realistic environment. Figure 46 shows a schematic of the concrete slab test with a fracture in one corner and an array of accelerometer holes at various distances from the fracture. Explosive pellets would be loaded in the fracture, embedded in sand, surrounded by water and covered by a weight to tamp the materials in the fracture.

Accerometers were newly purchased Endevco Isotron accelerometers, including both tri-axial units (65-10) and single accelerometers (2250A-10). Response curves for these accelerometers are shown in Figures 47 and 48. These accelerometers were to be potted in their holes using cement similar to the concrete slab. Instrumentation electronics included battery-powered constant-current-source/amplifier modules available from previous applications and recording oscilloscopes available at the explosive testing facility.

Unfortunately, after weeks of trying, the project was not able to obtain the necessary Air Force permit to construct the slab before the end of the project lifetime (Sept 25, 2003) and no final field test was performed.

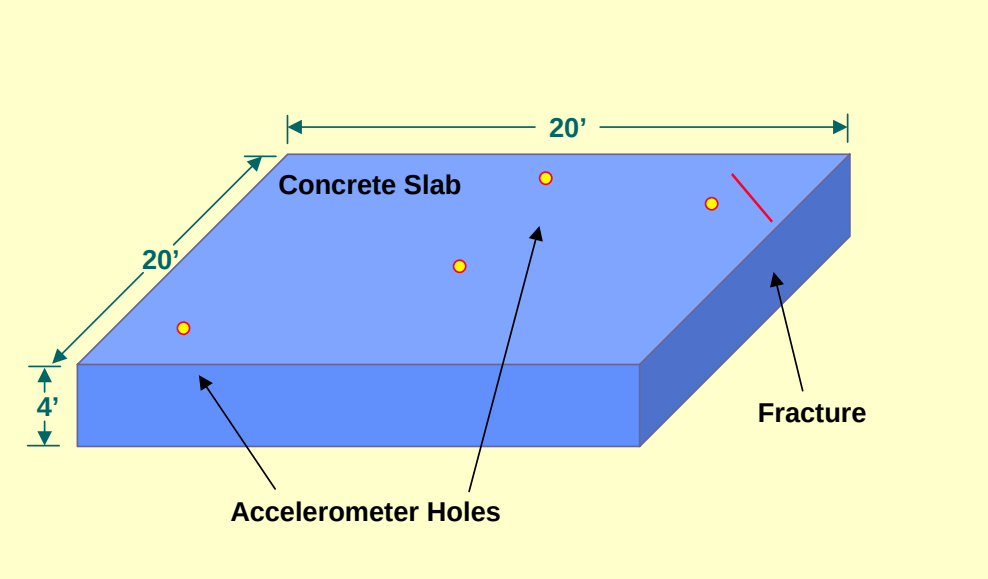

Figure 46. Schematic of concrete slab test.

65-10 Accelerometer Response

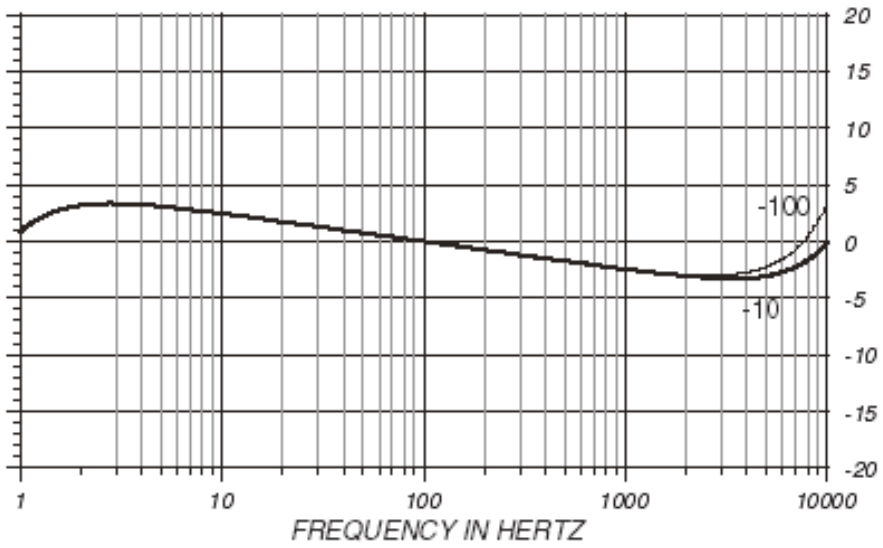

Figure 47. Endevco Isotron 65-10 accelerometer response curve.

2250A-10 Accelerometer Response

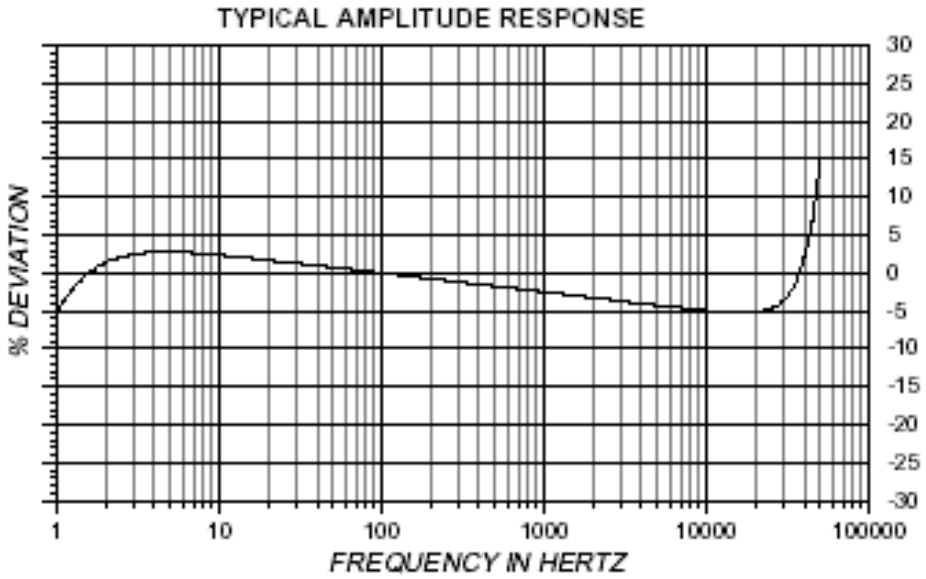

Figure 48. Endevco Isotron 2250A-10 accelerometer response curve.

Conclusions

In summary, this report detailed an effort to develop an autonomous micro-explosive for use in hydraulic fracturing. It began with an investigation of energetic materials that are likely to be suitable for this application, with particular emphasis on finding an energetic material that would react with water at a sufficiently rapid rate to produce a fast pressure pulse that would be imparted on the side walls of a hydraulic fracture. Magnesium silver nitrate was found to be the best candidate for this material. While a reaction between the energetic material and the water in the fracture (after dissolving or breaking a seal) was the simplest concept, a parallel study was also started to look at triggering devices. Several potential low-power SCB devices were built and tested, along with a power source and timer to fire the device at the appropriate time. Elements of package shape and flow through the fracture were also considered and it was found that the non-Newtonian properties of typical fracture fluids allowed for torpedo shapes to be used because the torpedoes would align with the flow stream. Calculations were made on the amount of energy that would be coupled into the rock using an elastic wave code, and results showed that relatively high amounts of energy would be imparted into the rock. A concrete block test that would have provided a final ground truth assessment of the technology was never carried out because of difficulty in obtaining an Air Force permit.

Specifically, the concept of autonomous microexplosive tracers has been investigated from materials, firing, energy, and size/shape aspects. Although the concept is clearly valid for some range of fracture sizes and sufficient development of this technology has been demonstrated to show engineering practicality, the sizes of the particles that would be needed for use in the majority of hydraulic fracture tests may be somewhat smaller than an optimum design of the pellets would allow. However, the energy coupling of the pellet with the formation through a crack was never directly tested because of the inability to obtain concrete-block results. Thus the minimum size of the pellets can only be inferred from other measurements.

Clearly, energetic materials for both reactive and timed trigger systems have been identified and either system can be constructed at this time. For water-reactive systems, a water-soluble coating slowly dissolves and results in contact of the reactive material (magnesium silver nitrate) with water. This material could either be the entire energetic package or could be used to detonate an explosive material. For the timed system, the SCB ignites the explosive of choice directly. The major issues with the timed system that have not been fully evaluated are the energy source and the timer for a fully miniaturized system.

Calculations suggest that sufficient energy can be generated and coupled to the formation so that reasonable monitoring distances (e.g., hundreds of meters) can be employed. The major uncertainty at this time is the frequency content of the seismic energy. Higher frequencies produce very large accelerations, but higher frequencies also attenuate faster in typical rocks. An optimum range, and hence an optimum rise time for the energetic material, has not been explicitly found since the concrete block test was not completed.

This page intentionally left blank.

References

1. Howard, G.C. and Fast, C.R., *Hydraulic Fracturing*, SPE Monograph Volume 2, Dallas, 1970.
2. Gidley, J.L., Holditch, S.A., Nierode, D.E., and Veatch, R.W., "*Recent Advances in Hydraulic Fracturing*, SPE Monograph Volume 12, Richardson, TX, 1989.
3. Economides, M.J. and Nolte, K.G., "*Reservoir Stimulation, 3rd Edition*, John Wiley and Sons, New York, 2000.
4. Warpinski, N.R., Branagan, P.T., Peterson, R.E., Wolhart, S.L. and Uhl, J.E., "Mapping Hydraulic Fracture Growth and Geometry Using Microseismic Events Detected by a Wireline Retrievable Accelerometer Array," SPE 40014, Proceedings, SPE Gas Technology Symposium, Calgary, Alberta, Canada, March 15-18, 1998.
5. *FracPac Completion Services*, Halliburton Energy Services, Houston, TX 1994.
6. Aldridge, D.F., "Radiation of Elastic Waves from Point Sources in a Uniform Wholespace," Sandia National Laboratories Report, SAND2000-1767, July 2000.
7. Huang, P.Y., Hu, H.H. and Joseph, D.D., "Direct Simulation of the Sedimentation of Elliptic Particles in Oldroyd-B fluids," *Journal of Fluid Mechanics*, **362**, pp. 297-325, 1998.
8. Patankar, N.A., Joseph, D.D., Wang, J., Barree, R.D., Conway, M. and Asadi, M., "Power-Law Correlations for Sediment Transport in Pressure Driven Channel Flows," *International Journal of Multiphase Flow*, **28**, pp. 1269-1292, 2002.
9. Wang, J., Joseph, D.D., Patankar, N.A., Conway, M. and Barree, R.D., "Bi-Power Law Correlations for Sediment Transport in Pressure Driven Channel Flows," *International Journal of Multiphase Flow*, **29**, pp. 475-494, 2003.
10. Feng, J., Joseph, D.D., Glowinski, R. and Pan, T.W., "A Three-Dimensional Computation of the Force and Torque on an Ellipsoid Settling Slowly through a Viscoelastic Fluid," *Journal of Fluid Mechanics*, **283**, pp. 1-16, 1995.
11. Prud'homme, R.K., "Rheology of Fracturing Fluid Slurries", GRI Report under Contract 5089-211-1880, Princeton University, 1991.
12. Aldridge, D.F., personal communication regarding use of the ELASTI code, 2002.

DISTRIBUTION

1	MS 0603	S.H. Kravitz, 1763
1	0603	J. Nogan, 1763
1	0701	P.B. Davies, 6100
1	0750	. Elbring, 6116
1	0750	B.P. Engler. 6116
1	0750	J.E. Uhl, 6116
5	0750	N.R. Warpinski, 6116
1	0839	M.C. Grubelich, 16000
1	1073	G.R. Dulleck, 1738
1	1156	R.R. Rivas, 15322
1	1156	P.W. Cooper, 15322
1	1452	B.V. Ingram, 2552
1	1452	B.M. Melof, 2552
1	9018	Central Technical Files, 8945-1
2	0899	Technical Library, 9616
1	0161	Patent and Licensing Office, 11500
1	0188	D. Chavez, LDRD Office, 1030